

QUASAR OUTFLOWS AND AGN FEEDBACK IN THE FAR UV: HST/COS OBSERVATIONS OF QSO HE0238–1904*

Nahum Arav¹, Benoit Borguet¹, Carter Chamberlain¹, Doug Edmonds¹, Charles Danforth²,

Received _____; accepted _____

*Based on observations made with the Hubble Space Telescope

¹Department of Physics, Virginia Tech, Blacksburg, VA 24061: arav@vt.edu

²CASA, University of Colorado, 389 UCB, Boulder, CO 80309-0389

ABSTRACT

Spectroscopic observations of quasar outflows at rest-frame 500Å–1000Å have immense diagnostic power. We present analyses of such data, where absorption troughs from three important ions are measured: first, O IV/O IV* that allow us to obtain the distance of high ionization outflows from the AGN; second, Ne VIII and Mg X that are sensitive to the very high ionization phase of the outflow. Their inferred column densities, combined with those of troughs from O VI, N IV, and H I, yield two important results: 1) The outflow shows two ionization phases, where the high ionization phase carries the bulk of the material. This is similar to the situation seen in x-ray warm absorber studies. Furthermore, the low ionization phase is inferred to have a volume filling factor of $10^{-5} - 10^{-6}$. 2) From the O IV*/O IV column density ratio, and the knowledge of the ionization parameter, we determine a distance of 3000 pc from the outflow to the central source. Since this is a typical high ionization outflow, we can determine robust values for the mass flux and kinetic luminosity of the outflow: $40 M_{\odot} \text{ yr}^{-1}$ and $10^{45} \text{ ergs s}^{-1}$, respectively, where the latter is roughly equal to 1% of the bolometric luminosity. Such a large kinetic luminosity and mass flow rate measured in a typical high ionization wind suggests that quasar outflows are a major contributor to AGN feedback mechanisms.

Subject headings: galaxies: quasars — galaxies: individual (QSO HE0238–1904) — line: formation — quasars: absorption lines

1. INTRODUCTION

Quasar outflows are detected as UV absorption troughs blueshifted with respect to the AGN’s rest frame spectrum. The ubiquity and wide opening angle deduced from the detection rate of these mass outflows, allows for efficient interaction with the surrounding medium. The energy, mass, and momentum carried by these outflows are thought to play an important role in shaping the early universe and dictating its evolution (e.g. Scannapieco & Oh 2004; Levine & Gnedin 2005; Hopkins et al. 2006; Cattaneo et al. 2009; Ciotti et al. 2009, 2010; Ostriker et al. 2010). Theoretical studies and simulations show that this so-called AGN feedback can provide an explanation for a variety of observations, from the chemical enrichment of the intergalactic medium, to the self-regulation of the growth of the supermassive black hole and of the galactic bulge (e.g. Silk & Rees 1998; Di Matteo et al. 2005; Germain et al. 2009; Hopkins et al. 2009; Elvis 2006, and references therein).

In order to assess this contribution quantitatively, we initiated a research program to determine the mass flow rate (\dot{M}) and kinetic luminosity (\dot{E}_k) of the outflows. We began by analyzing data from low-ionization outflows (showing Fe II/Fe II* and Si II/Si II* troughs: (Arav et al. 2008; Korista et al. 2008; Moe et al. 2009; Dunn et al. 2010b; Bautista et al. 2010; Aoki et al. 2011; Borguet et al. 2012b). While doing so we built upon ours (de Kool et al. 2001, 2002b,a) and other groups (Wampler et al. 1995; Hamann et al. 2001) previous investigations of such outflows. As we discuss below, the rarity of these low-ionization outflows put a significant uncertainty on the extrapolation of their results to the majority of quasar outflows, which show higher ionization species. Therefore, we recently started analyzing outflows that show troughs from the high ionization Si IV/Si IV* species (Dunn et al. 2012; Borguet et al. 2012a). Where we had to overcome the difficulty of these troughs being heavily contaminated by intervening Ly α forest absorption in spectra of high redshift quasars. These efforts yielded the most energetic BALQSO outflow measured to date, with a kinetic luminosity of at least 10^{46} ergs s $^{-1}$, which is 5% of the bolometric

luminosity of that high Eddington ratio quasar (Borguet et al. 2013).

In this paper we explore another promising part of the spectrum for quasar outflow science, the rest-frame $500 - 1000 \text{ \AA}$. Earlier studies of quasar outflows in this spectral regime utilized some of the diagnostic power of this band (e.g., Q 0226–1024, Korista et al. 1992; UM 675, Hamann et al. 1995; Q SBS 1542+541, Telfer et al. 1998; PG 0946+301, Arav et al. 1999b, Arav et al. 2001b; J2233–606, Petitjean & Srianand 1999; 3C 288.1, Hamann et al. (2000); HE 0226–4110, Ganguly et al. 2006). However, the UV spectrographs used in these works lacked the combination of spectral resolution and sensitivity that allows the full diagnostic potential of outflow absorption troughs to be used (see Section 2.2). For example, none of these studies were able to measure the distance of the outflows from the central source, which is crucial for determining the relationship between the outflow and the host galaxy.

The Cosmic Origins Spectrograph (COS) onboard the Hubble Space Telescope (HST) has improved this situation dramatically. We can now obtain high enough quality data on bright, medium-redshift quasars ($1.5 \gtrsim z \gtrsim 0.5$) to allow for detailed and reliable analysis of quasar-outflows spectra in this regime. Pioneering work on such data was done by Muzahid et al. (2012, hereafter M2012) who analyzed high resolution HST/COS observations (supplemented by FUSE archival data) of quasar HE0238–1904. Their main finding was that the outflowing gas must have two ionization phases. Here we detail a careful reanalysis of the same data set, where we are able to: a) detect absorption features associated with O IV^* , which allows us to determine the distance, \dot{M} and \dot{E}_k of the outflow and b) better quantify the two ionization phases of the outflow and put limits on its metallicity.

The plan of this paper is as follows: In Section 2 we discuss the diagnostic power of troughs from the rest wavelength between $500 - 1000 \text{ \AA}$ compared with those of longward wavelength troughs. COS observations of HE0238–1904 and the absorption troughs’ characterization are described in Section 3 and Section 4. The troughs’ column

density measurements are described in Section 5. Photoionization modeling is discussed in Section 6, and the energetics of the outflow in Section 7. In Section 8 we elaborate on the two-phase nature of the outflow, determine its distance from the central source, and derive the \dot{M} and \dot{E}_k of the outflow. We discuss our results in Section 9 and summarize them in Section 10.

2. DETERMINING THE PHYSICAL CONDITIONS AND ENERGETICS OF QUASAR OUTFLOWS

2.1. From Absorption Spectrum To Kinetic Luminosity Determination

Assuming the outflow is in the form of a partial thin spherical shell ($\Delta R/R \lesssim 1/2$) moving with velocity v , its mass (M), mass flow rate (\dot{M}) and kinetic luminosity (\dot{E}_k) are given by (see discussion in Borguet et al. 2012b):

$$M \simeq 4\pi\Omega R^2 N_H \mu m_p \quad \dot{M} \equiv \frac{M}{(R/v)} = 4\pi\Omega R N_H \mu m_p v \quad \dot{E}_k = \frac{1}{2} \dot{M} v^2, \quad (1)$$

where Ω is the fraction of the total solid angle occupied by the outflow, R is the distance of the outflow from the central source, N_H is the total hydrogen column density of the outflow, m_p is the mass of the proton and $\mu = 1.4$ is the molecular weight of the plasma per proton. We note that \dot{M} is the average mass flow rate over the dynamical time-scale (R/v).

To measure the quantities given in equation (1) the following steps are needed:

1. Measuring reliable ionic column densities (N_{ion}) from the observed troughs (see Section 5).
2. Photoionization modeling to determine N_H and the ionization parameter (U_H) from the measured N_{ion} (Section 6).
3. Determining R : a) measuring the number density (n_H) via troughs from metastable levels (Section 5) and b) using the inferred n_H and U_H to solve for the distance of the absorbing gas (Section 7).
4. Constraining the solid angle Ω of the outflow (Section 7).

5. Measuring or constraining the chemical abundances (Section 6).

The last variable v , is easily measured from the Doppler shift of the absorption trough with respect to the systemic redshift of the quasar.

Over the past decade significant advancements were made on all these steps **1.** (Arav 1997; Arav et al. 1999b,a, 2002, 2005, 2008, 2012; Hamann et al. 1997; de Kool et al. 2002b; Gabel et al. 2003, 2005b; Moe et al. 2009), **2.** (Arav et al. 2001b,a, 2007; Gabel et al. 2005a; Korista et al. 2008; Edmonds et al. 2011) **3.** (de Kool et al. 2001; Hamann et al. 2001; de Kool et al. 2002b,a; Moe et al. 2009; Dunn et al. 2010b; Bautista et al. 2010; Borguet et al. 2012b, 2013) **4.** (Hewett & Foltz 2003; Ganguly & Brotherton 2008; Dai et al. 2008; Knigge et al. 2008; Dunn et al. 2012; Dai et al. 2012), and **5.** (Arav et al. 2001a, 2007; Gabel et al. 2006; Moe et al. 2009; Borguet et al. 2012a).

However, due to astrophysical and instrumental constraints, most of these investigations dealt with Ly α (1215Å) and longer wavelength absorption troughs, while a small number of low luminosity and low redshift objects were studied down to 1000Å rest wavelength. Unfortunately, the rest wavelength $\gtrsim 1000$ Å is rather limited in spectral diagnostics for two important aspects of the outflows.

First, the highest ionization species available at these wavelength is O VI. This does not allow us to probe the higher ionization material that is known to exist in these outflows via x-ray observations. For example, the Chandra/FUSE/HST-STIS campaign on Mrk 279 found clear evidence for two ionization components in the outflow separated by roughly a factor of a hundred in ionization parameter. Only the low ionization phase was detected in the UV observations (which covered O VI absorption), where the independent UV and x-ray analyses were in very good agreement for the N_H and U_H of this component (Costantini et al. 2007; Arav et al. 2007). The higher ionization phase, which was only detected in the x-rays, contained 3 times larger N_H (Costantini et al. 2007). Such separate ionization components are typical for x-ray warm absorbers, where in some cases the higher ionization x-ray phase has 10 times or more N_H than the lower ionization UV phase. For

example, from Table 3 in Gabel et al. (2005a), in the NGC 3783 outflow the combined column density of the warm absorber is 10-20 times higher than that detected in the UV components. It is clear from Equation (1) that missing 90% of the outflowing column density will severely underestimate the \dot{M} and \dot{E}_k of the outflow.

Second, to determine R we need to measure the n_H of the outflow. This necessitates analyzing troughs from excited or metastable levels, combined with resonance troughs from the same ion (see § 5). Most quasar outflows show troughs from only triply or higher ionized species (with the exception of H I). Lower ionization species are observed in only about 10% of the outflows (Dai et al. 2012). In this context, it is useful to divide the rest-wavelength UV band into three regions:

1) $\lambda > 1215$: longward of Ly α , contamination with intervening (mainly IGM) absorption features is small, and this is one reason why historically most spectroscopic studies of quasar outflows concentrated on this region. In this band, only a few ions have transitions from excited states and these are all from singly ionized species (C II, Si II and Fe II). Most of our previous determinations of R , \dot{M} and \dot{E}_k (as well as those of other groups, e.g., Hamann et al. 2001) came from these singly ionized species. Extrapolating from results based on singly ionized species to the majority of higher ionization outflows introduces two significant uncertainties for the inferred contribution of all outflows to AGN feedback: a) pure high ionization outflows may be at a different distance scale than those that show singly ionized species. b) Ω for the lower ionization outflows may be smaller than that of the high ionization outflows simply as a virtue of the former being detected less frequently. Alternatively, Hall et al. (2002); Dunn et al. (2010a) argue that Ω for both forms of outflows are the same and that the rarity of lower ionization outflows is due to line of sight effects. It is therefore important to directly obtain \dot{M} and \dot{E}_k of high ionization outflows in order to reduce the systematic uncertainty in the average Ω .

2) $1000 < \lambda < 1215$: this spectral region contains excited transitions from C III* (1175Å) and Si IV* (1072Å). In high-luminosity, high redshift quasars, troughs from these transitions can be severely contaminated with Ly α forest absorption features. In addition, the C III*

multiplet consists of 6 transitions that span a total of 1.5 \AA (less than 400 km s^{-1}), therefore absorption features from these transitions often self-blend. Despite these difficulties, the importance of these diagnostics to the analysis of quasar outflows, led us to pursue such troughs whenever possible (Dunn et al. 2012; Borguet et al. 2012a, 2013).

3) As we show in the next subsection and in Figure 1, the rest wavelength region between $500 - 1000 \text{ \AA}$ contains a far richer and more powerful set of outflow diagnostics; even more so when combined with the already available coverage of the $\lambda > 1000 \text{ \AA}$ spectral region.

2.2. Powerful Outflows Diagnostics in the Far UV (500–1000Å)

An in-depth physical analysis of quasar outflows necessitates a careful treatment of all the five steps mentioned in § 1. The starting point is the spectrum on hand with its instrumental quality (S/N and spectral resolution) and the diagnostic power of the detected outflow troughs. For the ubiquitous high ionization outflows (those that show troughs from only triply or higher ionized species), we noted in § 1 the dearth of useful troughs longwards of 1000 \AA . The situation is quite different for the $500\text{--}1000 \text{ \AA}$ band. In that spectral range we encounter many ionic transitions from high-ionization species which are detected as troughs in most quasar outflows. These troughs supply powerful combined diagnostics that have the potential to revolutionize our understanding of the connection between the outflow and the host galaxy and its surroundings. Figure 1 gives a visual representation to the more important ionic transitions available for quasar outflows.

2.2.1. Sensitivity to the warm absorber phase of the outflow

Much of what we have learned about AGN outflows come from the lithium like iso-sequence since they give rise to observed doublet troughs from C IV , NV and O VI at $\lambda_{rest} \gtrsim 1000 \text{ \AA}$. The same iso-sequence has similar doublet lines from progressively

higher-ionization abundant species shortwards of $\lambda_{rest} = 1000 \text{ \AA}$: Ne VIII $\lambda\lambda$ 770.409,780.324, Na IX $\lambda\lambda$ 681.719,694.146, Mg X $\lambda\lambda$ 609.793,624.941 and Si XII $\lambda\lambda$ 499.406,520.665. As we show in Section 6, Ne VIII and Mg X are sensitive to the same ionization parameter as the bulk of the material reported in detailed x-ray warm-absorber analysis (e.g. Gabel et al. 2005b; Costantini et al. 2007). For HE0238–1904, measurements of the doublets associated with these two ions yields enough information on the high ionization phase to show that in this object it carries ~ 100 times more mass and energy than the lower ionization phase.

2.2.2. *Eliminating the major uncertainty regarding Ω*

Shortwards of $\lambda_{rest} = 1000 \text{ \AA}$ there are several instances of resonance and excited troughs from the same high-ionization species, which produce outflow absorption troughs (e.g., N III/N III* $\lambda\lambda$ 989.799, 991.577; O IV/O IV* $\lambda\lambda$ 787.711, 790.199 and O IV/O IV* $\lambda\lambda$ 609.829, 608.397, more are displayed in Figure 1). As we show in Section 7, for HE0238–1904, measurements of O IV/O IV* $\lambda\lambda$ 787.711, 790.199 yield a distance of $R = 3000$ pc for the outflow. Since high-ionization outflows are the large majority of observed quasar outflows, we can take their detection frequency ($\simeq 50\%$ Ganguly & Brotherton 2008; Dai et al. 2008, and especially Muzahid et al. 2013) as a robust statistical average for the Ω of these outflows. This, removes the second major uncertainty discussed in the introduction.

2.2.3. *Separating abundances and photoionization effects*

To find the total column density (N_H) and the ionization parameter (U_H) of the absorbing material, we use photoionization models. The unknown chemical abundances of the absorbing gas introduces a significant uncertainty in these models when we use, as input, ionic column densities of different elements. For example, the same measured column densities for H I and O IV can yield a solution with very different N_H and U_H , for modest changes in the oxygen abundance, as the changes in N_H and U_H are highly non-linear with

the assumed abundances (as can be seen in Figure 8). This uncertainty can be largely removed by using column densities of more than one ion from the same element.

Unlike the longer wavelength band, the rest wavelength between 500 – 1000 Å contains several instances of resonance troughs from different ions of the same element. Such occurrences greatly reduce the errors in determining the photoionization equilibrium due to chemical abundance uncertainties (Arav et al. 2007) and dust depletion (Dunn et al. 2010b). For example, in the region $\lambda_{rest} > 1000\text{Å}$ we only detect troughs from one oxygen ion (O VI $\lambda\lambda$ 1031.926,1037.617) and usually obtain upper limits for O I λ 1302.17. In contrast, the rest 500–1000Å spectral region covers transitions from O II, O III, O IV and O V. Therefore, a full spectral coverage for $\lambda_{rest} > 500\text{Å}$ yields information from six oxygen ions. Similar situations occur for carbon, nitrogen, neon and sulfur. As we show in Section 6, for HE0238–1904 measurements, troughs from O IV and O VI are crucial for deciphering the ionization structure of the outflow.

2.2.4. *Measuring reliable ionic column densities*

Reliable measurements of the absorption ionic column densities (N_{ion}) in the troughs are crucial for determining almost every physical aspect of the outflows: ionization equilibrium and abundances, number density, distance, mass flow rate and kinetic luminosity. Our group (Arav 1997; Arav et al. 1999b,a; de Kool et al. 2001; Arav et al. 2001b,a, 2002, 2003; Scott et al. 2004; Gabel et al. 2005b) and others (Barlow et al. 1997; Telfer et al. 1998; Churchill et al. 1999; Ganguly et al. 1999) have shown that outflow troughs often exhibit non-black saturation. Therefore, traditional absorption method techniques (apparent optical depth, equivalent width and curve of growth) often severely underestimate the true N_{ion} . A major improvement is achieved by using resonance doublet lines that allow fitting more sophisticated models, mainly a pure partial covering model, or an inhomogeneous model (e.g. Arav et al. 2005). However, both of these models have two free parameters, and we can usually find a perfect fit for either model given an unblended doublet trough. In a

few cases we were able to fit more than two lines from the same ion and thus determine which model gives a better fit to the data. To date, the few published analyses to this end (e.g. Arav et al. 2008; Borguet et al. 2012b) used low ionization species (mainly Fe II and Si II).

Extending the spectral coverage to 500 – 1100 Å yield several ionic species with multiple resonance transitions. The most important of these is the H I Lyman series. It serves both as a very sensitive measure of the true N_H as well as the best probe for the chemical abundances of the outflow (when compared with N_{ion} of heavier elements). Other useful examples are: O VI 787.7105Å, 608.3968Å, 554.0756Å, 553.3293Å with more than a spread of 3 in oscillator strength (f); S IV 1062.6640Å, 809.6556Å, 744.9045Å, 657.3187Å with more than a spread of 20 in f .

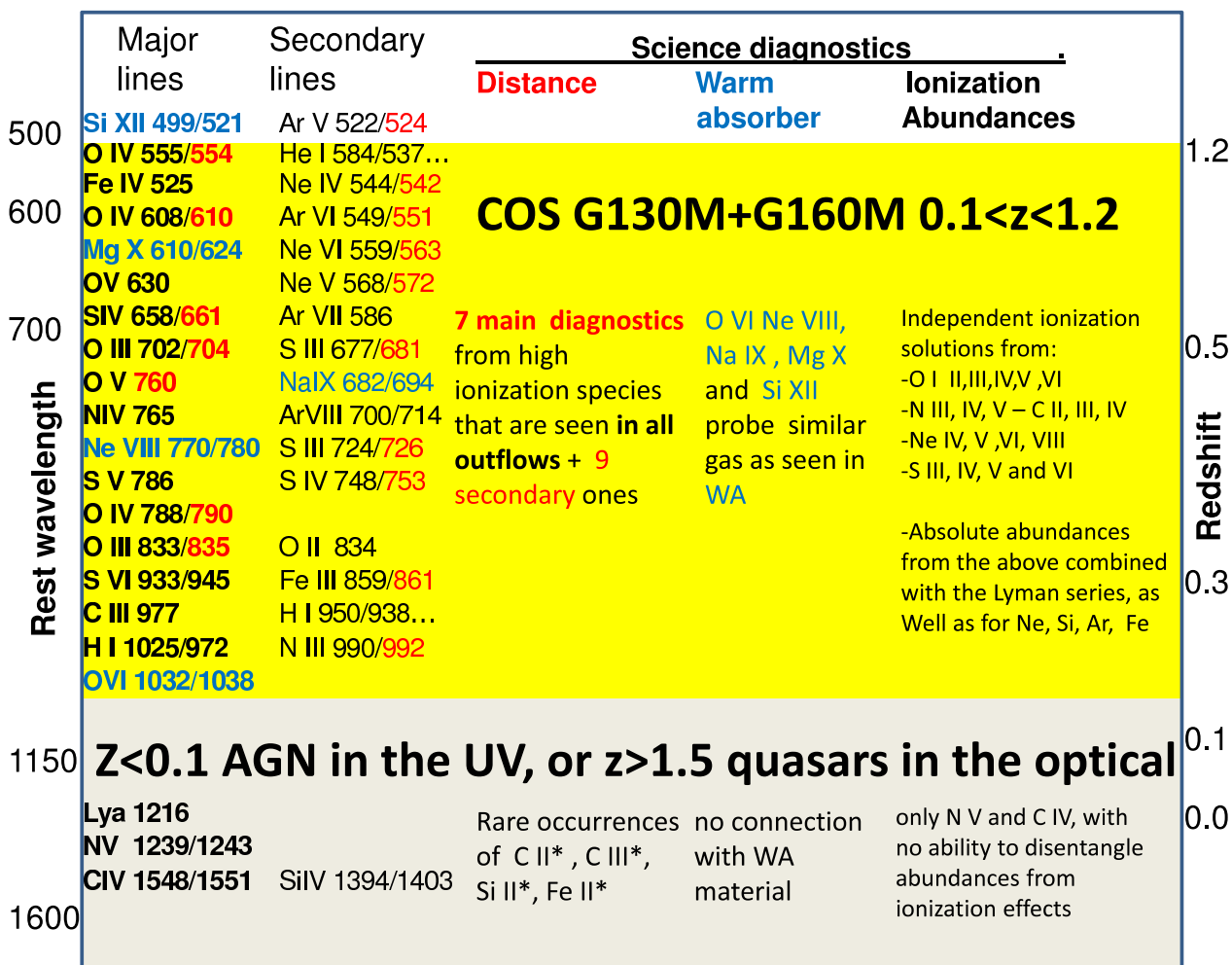


Fig. 1.— With 20 times higher throughput in the FUV than STIS Echelle, COS G130M and G160M gratings can observe quasars at the $0.1 < z < 1.3$ range with sufficient S/N and resolution to extract outflow science. This opens up the spectral-diagnostics-rich 500–1050Å rest-frame region (yellow band). The left two columns show the lines observed as absorption troughs in quasar outflows. In the right three columns we show the use of these lines as physical diagnostics in the three main analysis areas: a) distance to the outflows is determined by using absorption from excited states (noted in red); b) direct connection to the x-ray warm absorber is achieved by observing very high ionization lines (noted in blue); c) ionization equilibrium and abundances effects are separated their by analyzing absorption from multiple ions from the same element and measuring several lines from the Lyman series.

3. DATA OVERVIEW

3.1. Observations and data reduction

The quasar HE 0238–1904 was observed with HST/COS (see Osterman et al. 2010, for on-orbit performance) on 2009 December 31. Spectra of the target were obtained using the Primary Science Aperture (PSA) in both the G130M ($1135 < \lambda < 1480 \text{ \AA}$) and G160M ($1400 < \lambda < 1795 \text{ \AA}$) medium-resolution ($R = \lambda/\Delta\lambda \approx 18,000$) gratings as part of the COS Guaranteed Time Observations (GTO) program (PI: Green, PID: 11541) and totaled 6451 s and 7487 s in the G130M and G160M gratings, respectively. Both sets of observations used multiple grating central settings in order to provide a continuous spectral coverage across the entire COS far-UV band as well as dither instrumental features in wavelength space.

Each dataset is reduced with the COS calibration pipeline CALCOS v2.11f. Flat-fielding, alignment and co-addition of the processed exposures is then carried out using IDL routines developed by the COS GTO team specifically for COS FUV data¹ and described in Danforth et al. (2010). Briefly, each exposure is corrected for narrow, $\sim 15\%$ -opaque, shadows from repeller grid wires. The local exposure time in these regions was reduced to give them less weight in the final co-addition. Similarly, exposure times for data at the edges of the detectors was de-weighted. With multiple central wavelength settings per grating, any residual instrumental artifacts from grid-wire shadows and detector boundaries have negligible effect on the final spectrum.

Next, strong ISM features in each exposure are aligned via cross-correlation and interpolated onto a common wavelength scale. The wavelength shifts are typically on the order of a resolution element ($\sim 15 \text{ km s}^{-1}$) or less. The co-added flux at each wavelength is taken to be the exposure-weighted mean of flux in each exposure. To quantify the quality of the combined data, we identify line-free continuum regions at various wavelengths, smooth

¹IDL routines available at <http://casa.colorado.edu/~danforth/costools.html>

the data by the seven-pixel resolution element and define $S/N \equiv F/\Delta F \approx 20 - 25$ in the data, where ΔF is the standard deviation of the flux. In Fig. 2 we present sections of the fully reduced COS spectrum along with the identification of intrinsic absorption troughs.

3.2. Unabsorbed emission model

Determining the column density associated with each ion requires the knowledge of the unabsorbed emission model $F_0(\nu)$. The typical AGN emission is comprised of three main sources: a continuum emission, a broad emission line component (BEL) and a narrow emission line component (NEL). We model the de-reddened ($R_V = 3.1$, $E(B - V) = 0.032$ (Schlegel et al. 1998)) continuum emission of HE0238-1904 using a single power law of the form $F_{(\lambda)} = F_{1100}(\lambda/1100)^\alpha$. A χ^2 minimization of the model over regions free of known emission/ absorption lines gives an overall good fit with parameters $F_{1100} = 1.714 \times 10^{-14} \pm 0.008 \times 10^{-14}$ and $\alpha = -0.234 \pm 0.043$.

The emission line profiles in the HE0238-1904 spectrum are generally smooth and shallow. We fit the prominent O VI emission using two broad gaussians of $FWHM \sim 4000$ and ~ 12000 km s $^{-1}$ for the BEL and a single NEL with $FWHM \sim 700$ km s $^{-1}$ centered on each line of the doublet. The remaining weaker emission features are modelled by a spline fit. In Fig. 3, we present the unabsorbed emission model we constructed over the O VI and Ne VIII regions of HE0238-1904.

4. ABSORPTION TROUGHS CHARACTERISATION

4.1. Identification of intrinsic absorption features

The COS FUV spectrum of HE0238-1904 ($z = 0.6309$) displays a variety of absorption features in part due to the interstellar medium in our galaxy (ISM); to a collection of intervening Lyman-alpha systems (IGM); and absorption features that are directly related

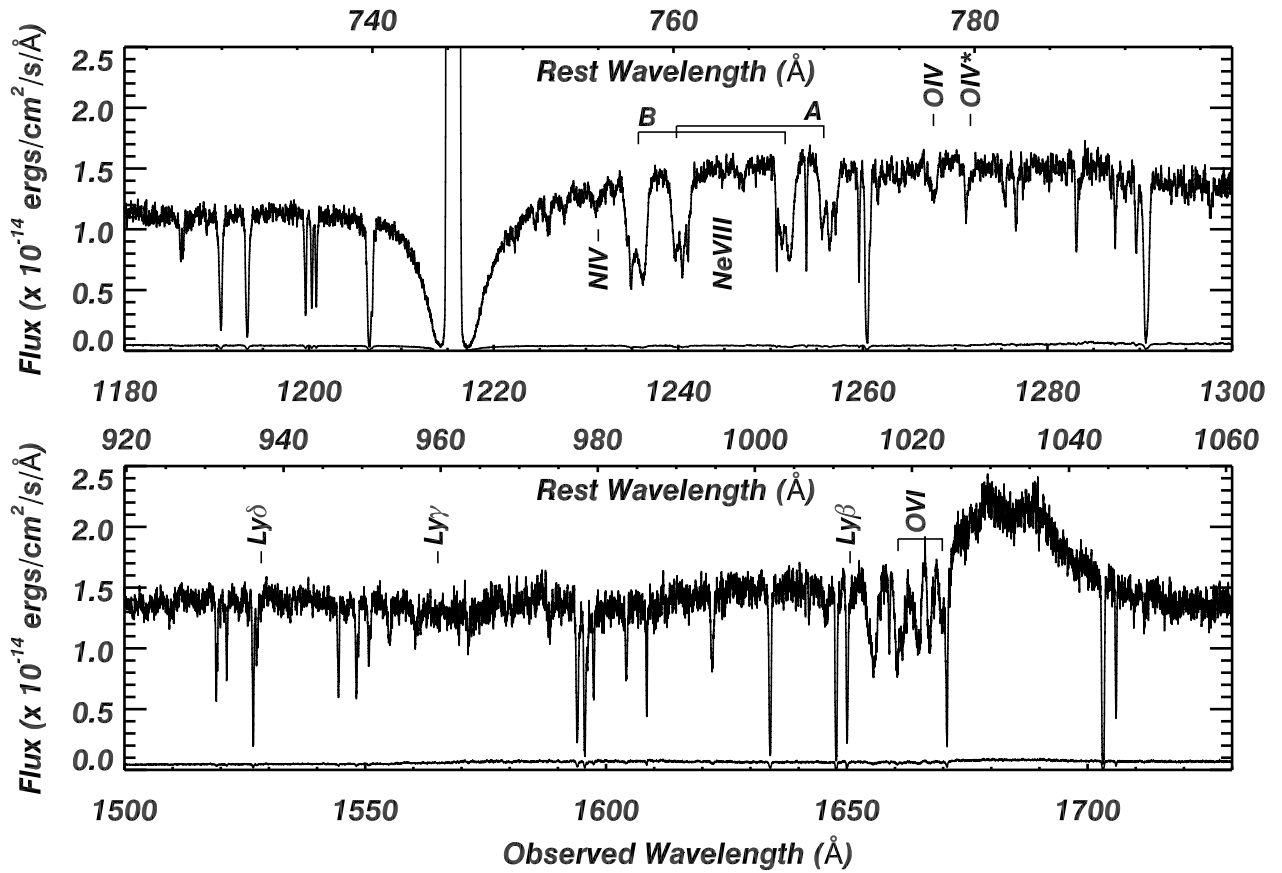


Fig. 2.— This figure presents over 80% of the fully reduced HE0238-1904 spectrum observed in December 2009 with HST/COS. The position of the main intrinsic absorption features are labeled.

to an intrinsic outflow from the quasar.

Using the line profile of the high ionization Ne VIII and O VI doublets as templates, we identify two main absorbing systems (A and B), blueshifted at velocities $v_A \sim -3850 \text{ km s}^{-1}$ and $v_B \sim -5000 \text{ km s}^{-1}$, both exhibiting a width $\Delta v \sim 500 \text{ km s}^{-1}$. The resolution of COS allows us to resolve each absorption system into several narrower components. System A exhibits three main subcomponents ($A1, A2, A3$) located at velocities $v_{A1} \sim -3698 \text{ km s}^{-1}$, $v_{A2} \sim -3835 \text{ km s}^{-1}$, $v_{A3} \sim -4026 \text{ km s}^{-1}$ while system B essentially displays two subcomponents ($B1, B2$) at velocities $v_{B1} \sim -4887 \text{ km s}^{-1}$, $v_{B2} \sim -5088 \text{ km s}^{-1}$ (see Fig. 3).

Using that kinematic structure template we identify absorption features associated with the outflow in lower ionization species such as N IV, O IV, and S VI as well as lines from the Lyman series ($\text{Ly}\beta$, $\text{Ly}\gamma$ and $\text{Ly}\delta$). The absorption detected in these ions are matching the kinematic structure of subcomponents $A3$ and $B1$, while displaying shallower troughs than the high ionization Ne VIII and O VI templates. An absorption feature associated with the $\lambda 790.199$ transition of excited O IV (O IV*) is detected in outflow component $A3$, while its blue wing is affected by a blend with an intervening Ly ϵ line.

The line of sight towards HE0238-1904 shows numerous intervening Lyman systems occasioning mild to severe blending of the diagnostic lines we use to characterize the properties of the intrinsic outflow. Using the strong Ly α and Ly β transitions, we identify at least 30 intervening Lyman systems in that direction (the analysis of these systems will be given in a future paper: Danforth et al. 2013). We detail the blends affecting each individual intrinsic absorption line and how we treat them in the next sections. The case of the O IV* line is of particular interest in our study, given that it allows us to estimate the density and hence the distance to the outflow.

Component $A3$ of the O IV* absorption line associated with the outflow of HE0238-1904 is observed at 1271.2 \AA , and is blended with Ly ϵ absorption from a strong IGM system at $z = 0.35548$ lying on its blue wing. Thanks to the broad spectral coverage and good data

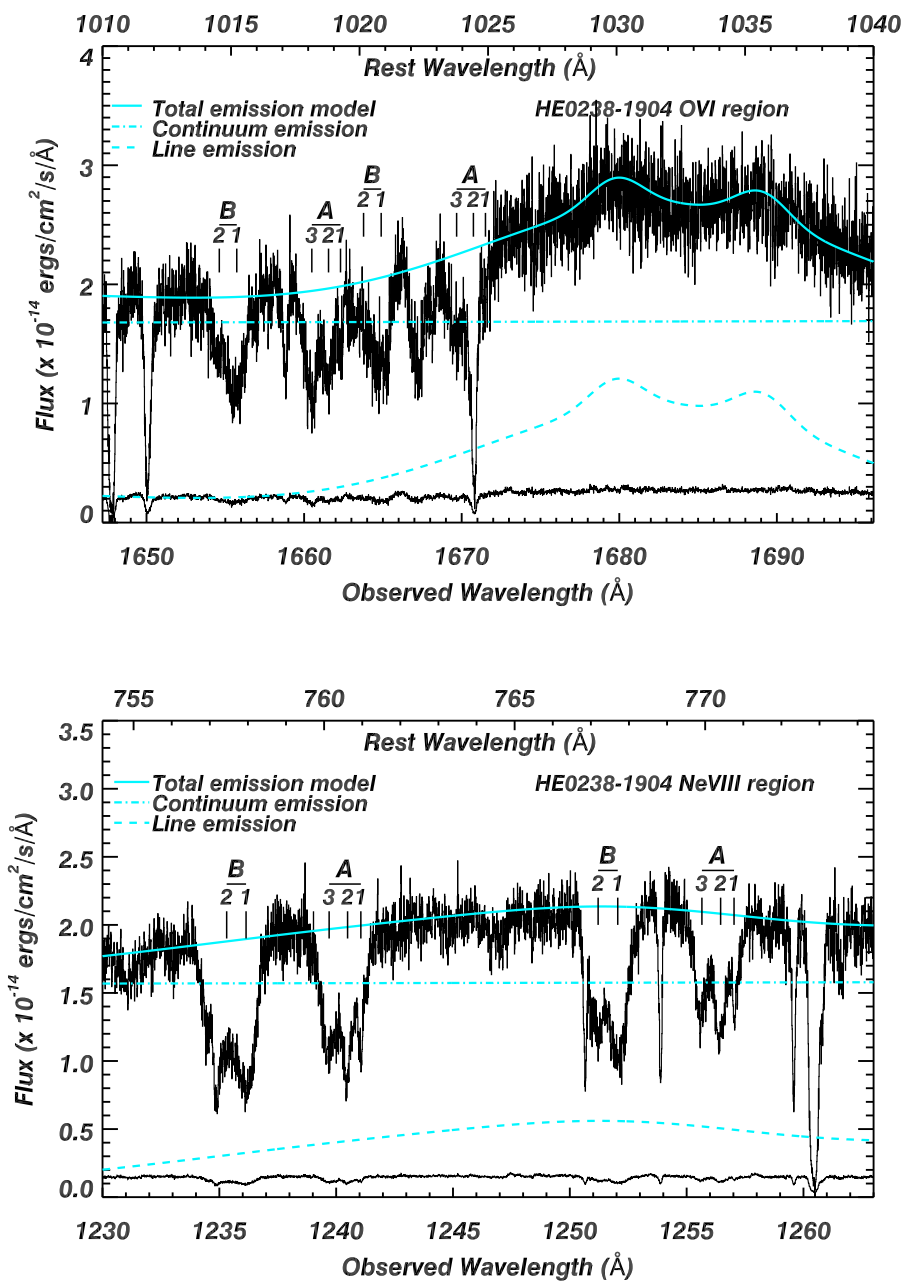


Fig. 3.— Detail of the unabsorbed emission model for the O VI and Ne VIII emission line region on the dereddened spectrum of HE0238-1904 (see text). The total emission model is plotted as a solid line on top of the data, the continuum contribution is plotted in dotted-dashed line and the line emission is plotted in dashed line. We also indicate the position of the absorbing systems identified from comparing the Ne VIII and O VI line profiles. The error spectrum is also shown at the bottom.

quality of the COS observations, we can model the H I absorption out fairly accurately. We measured the equivalent widths of H I absorption in the $z = 0.35548$ system using the Ly α -Ly ζ transitions (excepting Ly ϵ). These equivalent widths were well-fit by a single curve-of-growth with parameters $\log N_{\text{HI}} = 14.95 \pm 0.05$ and $b_{\text{HI}} = 21 \pm 1 \text{ km s}^{-1}$. The constructed Ly ϵ trough model $M_{\text{Ly}\epsilon}(\lambda) = e^{-\tau_{\text{Ly}\epsilon}(\lambda)}$ was then divided out following the procedure $I_{\text{IGM-corrected}}(\lambda) = I(\lambda)/M_{\text{Ly}\epsilon}(\lambda)$, revealing the O IV* trough whose kinematic structure in trough A3 matches the one observed in the other ions of the outflow (see Fig. 4)

4.2. Inhomogeneities of the absorber

The column density associated with a given ion as a function of the radial velocity v is defined as:

$$N_{\text{ion}}(v) = \frac{3.8 \times 10^{14}}{f_j \lambda_j} \langle \tau_j(v) \rangle \quad (\text{cm}^{-2} \text{ km}^{-1} \text{ s}) \quad (2)$$

where f_j , λ_j and $\langle \tau_j(v) \rangle$ are respectively the oscillator strength, the rest wavelength and the average optical depth across the emission source of the line j for which the optical depth solution is derived (see Edmonds et al. 2011). The optical depth solution across a trough is found for a given ion by assuming an absorber model. As shown in Edmonds et al. (2011), the major uncertainty on the derived column densities comes from the choice of absorption model. In this study we investigate the outflow properties using column densities derived from three common absorber models.

Assuming a single, homogeneous emission source of intensity F_0 , the simplest absorber model is the one where a homogeneous absorber parameterized by a single optical depth fully covers the photon source. In that case, known as the apparent optical depth scenario (AOD), the optical depth of a line j as a function of the radial velocity v in the trough is simply derived by the inversion of the Beer-Lambert law : $\tau_j(v) = -\ln(F_j(v)/F_0(v))$, where $F_j(v)$ is the observed intensity of the line.

Early studies of AGN outflows pointed out the inadequacy of such an absorber model,

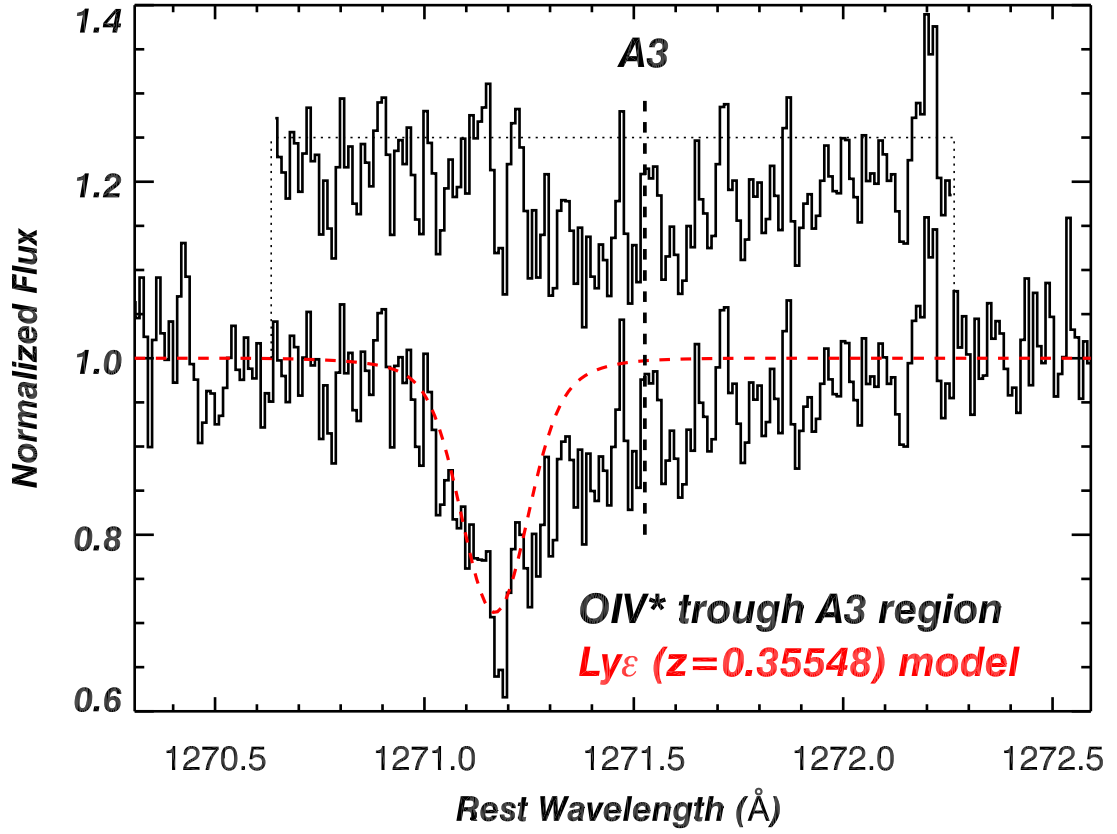


Fig. 4.— Deblending of component *A3* of the intrinsic O IV^* $\lambda 790.199$ by dividing out the $\text{Ly}\epsilon$ absorption model from the strong intervening system at $z = 0.35548$ (see text). The corrected normalized O IV^* profile, plotted here for clarity with a shifted continuum, matches the kinematic structure of other ions associated with the outflow.

specifically its inability to account for the observed departure of measured optical depth ratio between the components of typical doublet lines from the expected laboratory line strength ratio $R = \lambda_i f_i / \lambda_j f_j$. Two parameter absorber models have been developed to explain such discrepancies. The partial covering model (e.g. Hamann et al. 1997; Arav et al. 1999a, 2002, 2005) assumes that only a fraction C of the emission source is covered by absorbing material with constant optical depth τ . In that case, the intensity observed for a line j of a chosen ion can be expressed as

$$F_j(v) = F_0(v)(1 + C(v) * (e^{-\tau_j(v)} - 1)). \quad (3)$$

Our third choice are inhomogeneous absorber models. In that scenario, the emission source is totally covered by a smooth distribution of absorbing material across its spatial dimension x . Assuming the typical power law distribution of the optical depth $\tau(x) = \tau_{max} x^a$ (de Kool et al. 2002b; Arav et al. 2005, 2008), the observed intensity observed for a line j of a chosen ion is given by

$$F_j(v) = F_0(v) \int_0^1 e^{-\tau_{max,j}(v)x^{a(v)}} dx \quad (4)$$

Once the line profiles have been binned on a common velocity scale (we choose a resolution $dv = 20 \text{ km s}^{-1}$, slightly lower than the resolution of COS), a velocity dependent solution can be obtained for the couple of parameters (C, τ_j) or (a, τ_{max}) of both absorber models as long as one observes at least two lines from a given ion, sharing the same lower energy level. Once the velocity dependent solution is computed, the corresponding column density is derived using Equation 2 where $\langle \tau_j(v) \rangle = C_{ion}(v)\tau_j(v)$ for the partial covering model and $\langle \tau_j(v) \rangle = \tau_{max,j}(v)/(a_{ion}(v) + 1)$ for the power law distribution. Note that the AOD solution can be computed for any line (singlet or multiplet), without further assumption on the model, but will essentially give a lower limit on the column density when the expected line strength ratio observed is different from the laboratory value.

5. COLUMN DENSITY MEASUREMENTS

As mentioned in Section 4.1, the line of sight towards the quasar HE0238-1904, in addition to the usual interstellar medium lines, has many intervening Lyman systems affecting our ability to derive accurate ionic column density of lines associated with the intrinsic outflow, if not properly taken into account. In the following subsections we detail individually the blends affecting each intrinsic absorption troughs and present the analysis we performed in order to estimate the column density of each ion.

The compilation of measurements is presented in Table 1 in which the ionic column densities have been computed on four different sections of the main troughs A and B . The first three trough sections are related to absorption system A in which a clear signature of an excited state of O IV is detected in at least subtrough $A3$. Though the detection of O IV and O IV^* in $A3$ allows us to derive a distance to that component, the bulk of the column density comes from the total trough A . While the high velocity $v_A \sim -3850 \text{ km s}^{-1}$ and narrowness $\Delta v \sim 500 \text{ km s}^{-1}$ of the system suggests a physical connection between its subcomponents $A1$, $A2$ and $A3$, we further test the validity of that assumption by comparing the ionization solution for different sections of the main trough. The first integration range considered: $v_{A3} \in [-4050, -3930] \text{ km s}^{-1}$ is mainly centered on trough $A3$, but where the lower integration limit is chosen to avoid the blue wing of O IV^* , giving a measurement virtually independent of the correction of the $\text{Ly}\epsilon$ line blend. The second range consists of the remaining trough: $v_{A1+A2} \in [-3930, -3610] \text{ km s}^{-1}$, essentially comprising components $A1+A2$. The third range integrates the column density over the whole system A : $v_A \in [-4170, -3610] \text{ km s}^{-1}$. The last region, $v_B \in [-5270, -4650] \text{ km s}^{-1}$, simply integrate the column density over the whole higher velocity system B .

In Table 1 we compare the estimated column densities derived in the presented analysis and the values reported in the analysis of the same absorber in Muzahid et al. (2012). We summed the column densities reported in their paper and multiplied its value by the average covering of each species from their Table 1 in order to be consistent with the average values

we derive (see Section 4).

5.1. The Ne VIII troughs

We do not identify any blending in both components of the Ne VIII doublet in system *A* which allows us to derive a good column density solution over each subregion (v_A , v_{A1+A2} and v_{A3}) of the trough using the three absorber models described in Section 4. In system *B*, the blue wing of Ne VIII λ 780.324 line is blended between 1250 – 1251 Å by the ISM Si II λ 1250.578 line and also by a weak Ly ϵ IGM ($z = 0.3343$) line near 1251.2 Å. The blue wing of the blue component of Ne VIII λ 770.409 is affected by a blend with two Ly α IGM lines ($z = 0.0155$ and $z = 0.0158$) as well as a weak blend by a Ly γ IGM ($z = 0.2704$) line near 1235 Å. Given the different blending, a crude estimate of the Ne VIII column density is computed by using the three absorber solutions in the blend free region $v \in [-4750, -3650]$ km s $^{-1}$ and adding to it a lower limit on the column density that can be hidden in the blended region by scaling the optical depth solution of the non-blended O VI λ 1031.910 line template to the position of the Ne VIII λ 780.324 line.

5.2. The O VI troughs

The central part and the red wing of the O VI λ 1037.620 line in trough *A* are blended between 1670 – 1672 Å by the strong ISM Al II λ 1670.787 line. No blend is identified on the O VI λ 1031.910 trough. We checked the portion of the O VI λ 1037.620 affected by the blend by overplotting the unblended and non-saturated ISM Si II λ 1193.290 (with an ionization potential close to Al II) at the rest position of the Al II λ 1670.790 line, revealing that while the v_{A1+A2} region of O VI λ 1037.620 is the most affected section of the trough, the blend may still significantly affect the red part of the v_{A3} region. Taking that observation into account, we derive a lower limit on the ionic column density in region v_{A3} using the AOD method on O VI λ 1031.910. We estimate an upper limit for the same region by scaling the

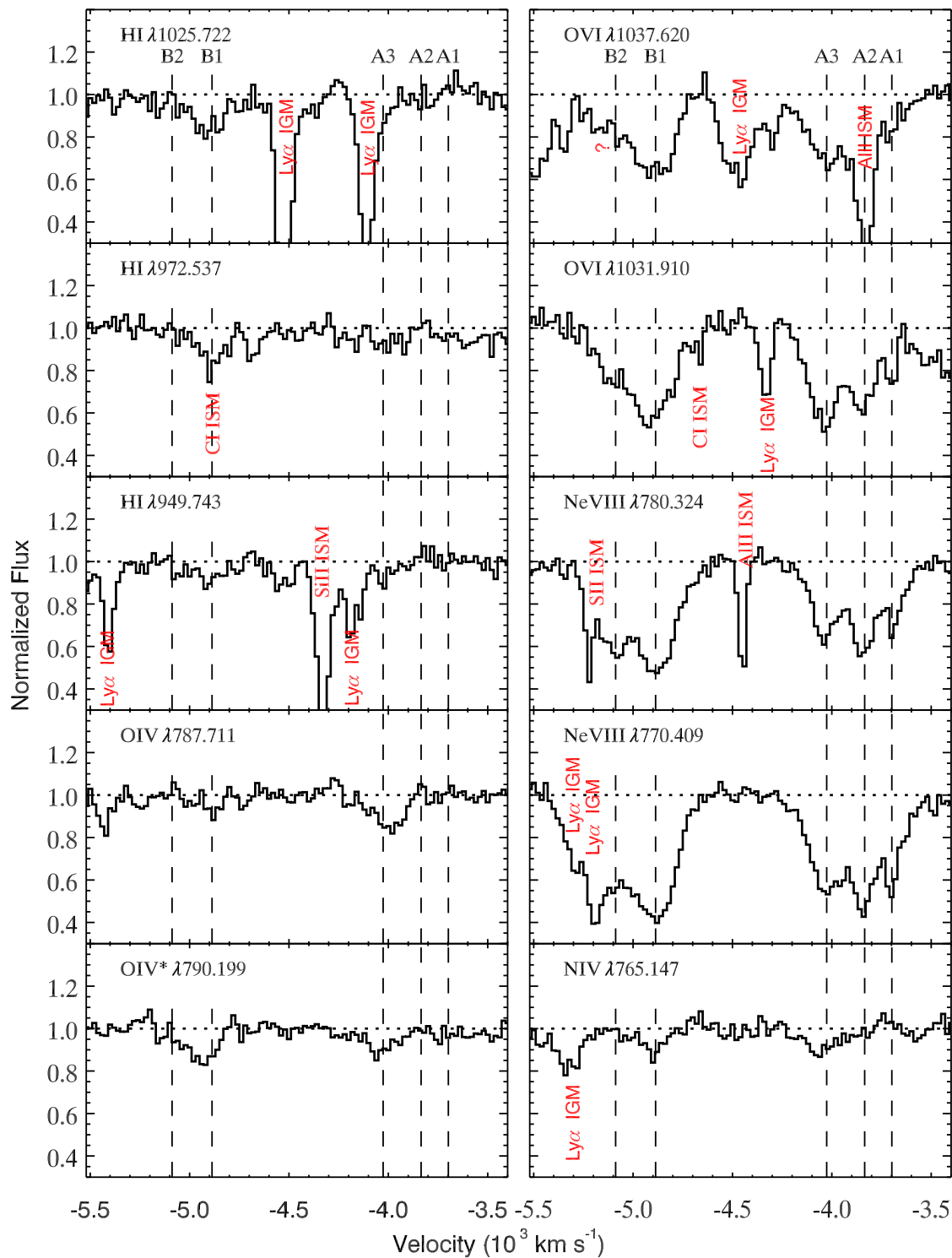


Fig. 5.— This figure presents the line profiles associated with ions identified in the outflow. the dashed line indicate the position of the outflow components. We label the blends affecting each line. The “?” in the top right panel corresponds to a probable unknown blend (see Section 5.2).

column density derived using the partial covering method over the unblended section of the region v_{A3} (ie. $v \in [-4050, -3970]$ km s⁻¹) to the entire v_{A3} trough width. In region v_{A1+A2} the strong blend of O VI $\lambda 1037.620$ only allow us to derive a lower limit on the column density by using the AOD method on the unblended O VI $\lambda 1031.910$ line.

Except for a weak blend by C I $\lambda 1656.929$ close to the red wing (but outside the v_B range) of O VI $\lambda 1031.910$, we do not a-priori identify any major blend in system B . However, the comparison of the residual flux in O VI $\lambda 1031.910$ and O VI $\lambda 1037.620$ strongly suggests a weak blend around 5200 km s⁻¹, since the residual flux in that component is in overall lower than the residual flux in the stronger O VI $\lambda 1031.910$ line. Taking that observation into account, we obtain an estimate of the column density using the three absorber model over the unblended section of the trough ($v \in [-4730, -5170]$ km s⁻¹) and adding the AOD contribution determined from the O VI $\lambda 1031.910$ line in the section where the unidentified blend affects O VI $\lambda 1037.620$ ($v \in [-5170, -5270]$ km s⁻¹). Note that in this first section of trough B , the power law method gives a larger amount of column density which is an artifact due to the inability of that absorber model to account for shallow, saturated ($I_{\lambda 1031.910} \sim I_{\lambda 1037.620}$) troughs (see Arav et al. 2005).

5.3. The H I troughs

We detect absorption troughs associated with neutral hydrogen in system A in Ly β , the overall S/N does not allow to assess the detection of absorption troughs in higher order lines. In region v_{A3} , the blue wing of the weak Ly β line is affected by a blend with a moderate IGM Ly α line at $z = 0.35733$. The absence of unblended higher order line for that IGM system prevent us to perform a curve-of-growth analysis of the system, so we modeled the IGM Ly α line by a gaussian profile centered around the rest Ly α in the $z = 0.35733$ frame and divided the model out. A lower limit of the H I column density in that region v_{A3} is then derived by scaling the AOD optical depth profile computed from the unblended Ne VIII $\lambda 770.409$ template to match the noisy Ly β residuals. A conservative upper limit on

H I is obtained in that same region by scaling the same template to the noise level for the Ly γ line. In region v_{A1+A2} , we estimate the H I column density by using the AOD method on the weak Ly β profile.

In system *B*, we identify H I troughs in the Ly β , Ly γ and possibly Ly δ lines. The only line suffering from known blending is Ly γ which is blended in the 1560 – 1561 Å region by the C I λ 1560.309 line. Given the shallowness of both Ly γ and C I lines as well as the limited S/N, we do not attempt to deblend these troughs and only use the Ly β and Ly δ lines to constrain the H I column density in that region. A conservative lower limit on H I is obtained by using the AOD method on the strong Ly β line while an upper limit is derived computing the AOD solution over the shallow Ly δ line region.

5.4. The O IV and O IV* troughs

A first look at the HE0238-1904 spectrum reveals the presence of absorption troughs associated with O IV λ 787.711 mainly in components *A3* and *B1*, while, once corrected for the IGM Ly ϵ $z = 0.35548$ blend (see Sect. 4.1), an absorption trough associated with O IV* λ 790.199 is detected mainly in component *A3*. Assuming no further blend, we can estimate the column density associated with these two states by using the AOD method on each of them, leading to an O IV column of $83.9^{+6.1}_{-5.9} \times 10^{12} \text{cm}^{-2}$ and $34.4^{+5.7}_{-5.1} \times 10^{12} \text{cm}^{-2}$ in region v_{A3} and v_{B1} respectively and an O IV* column of $49.5^{+7.1}_{-6.8} \times 10^{12} \text{cm}^{-2}$ in region v_{A3} .

A meticulous look at the O IV λ 787.711 line profile in trough *A3* however reveals a kinematic structure slightly different than the one observed in all the other species, showing an extended asymmetric red wing. That structure can be explained if that red wing is affected by a blend from an O IV* *B1* trough, as suggested in Fig. 6 in which we plot the expected position of the O IV and O IV* components based on the kinematic structure detailed in Section 4.1. In order to deblend the O IV *A3* and O IV* *B1* trough, we first modelled the unblended deep but non-saturated components *A3* and *B1* of the Ne VIII

λ 770.409 line by a simple gaussian, as suggested by the general profile of each component. Using a Levenberg-Marquardt minimization technique, we obtain a good fit to component *A3* with parameters $v_{cen} = -4026.22 \pm 4.56 \text{ km s}^{-1}$ and $FWHM = 275.27 \pm 17.17 \text{ km s}^{-1}$, where v_{cen} and $FWHM$ are the central position and Full Width at Half Maximum of the best gaussian model. For component *B1* we similarly derive $v_{cen} = -4887.04 \pm 3.45 \text{ km s}^{-1}$ and $FWHM = 325.61 \pm 13.46 \text{ km s}^{-1}$. Using the derived position and width of these two components, we construct a two component gaussian model of the O IV and O IV* blend once again using the same minimization technique. The best fitting model is presented in Fig. 6. Having computed a model of each trough inside the blend, we can correct the blended region in order to derive the actual column density in O IV* *B1* or O IV *A3* by dividing out the initial normalized line profile by the O IV or O IV* model. Applying this technique to the actual spectrum we obtain an AOD measurement in regions v_{A3} , v_B as well as v_{A1+A2} for both O IV and O IV* line, reported in Table 1.

5.5. Other intrinsic troughs

As mentioned in Section 4.1, we detect absorption features associated with other ionic species in the HE0238-1904 spectrum. The most prominent of them is N IV λ 765.147. No blends are identified in either system *A* or *B* for that line allowing us to derive a reliable AOD solution for the column density in these two components. A shallow signature is also probably detected in the strongest line of the S VI ion (i.e. S VI λ 933.376). While consistent with the overall noise level in that spectral range, we compute an upper limit on the S VI column density by deriving the AOD solution over systems *A* and *B*.

We also searched for other lower ionization lines like C III, N III and O III in order to better constraint the photoionization model of each absorber. The only feature identified for these ions is a possible signature of O III λ 832.927 in subcomponent *A3* which we also identified as a weak Ly β associated with the Lyman intervening system at $z = 0.3065$. We derive a conservative upper limit on the column density of each of these ions by scaling the

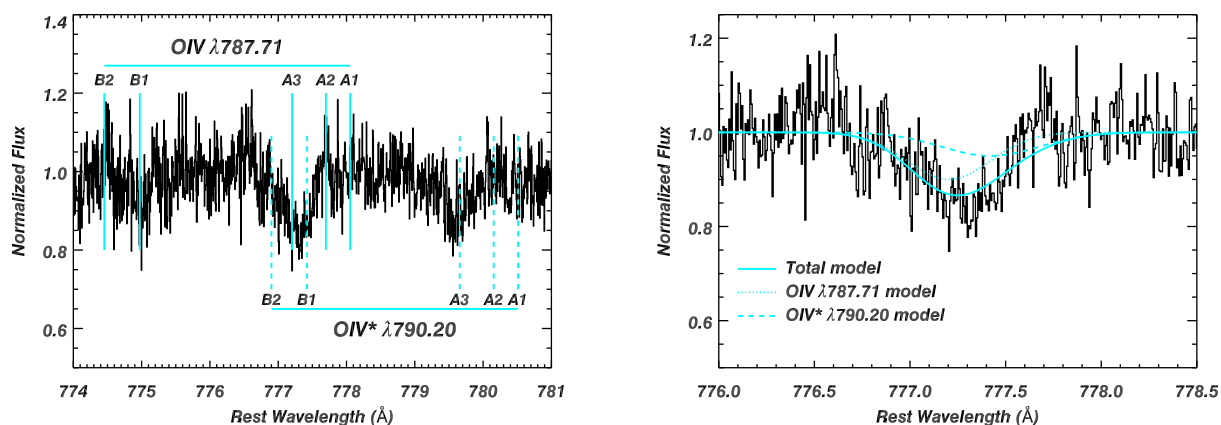


Fig. 6.— In the left panel we show the spectral region around the O IV* and O IV line on which we overplotted the position of each subcomponent, suggesting that the trough around the 777.25 Å rest-wavelength region is indeed a blend between O IV* B1 and O IV A3 troughs. In the right panel, we show our best fit to the blend assuming that each subtrough can be modeled by a single gaussian with parameters derived from the fit of strong unblended troughs of Ne VIII and O VI (see text for details).

optical depth template of the unblended Ne VIII λ 770.409 in regions v_{A1+A2} v_{A3} and v_A and the template of O VI λ 1031.910 in region v_B .

5.6. FUSE archival data

HE0238-1904 has been observed by the Far Ultraviolet Spectroscopic Explorer telescope (FUSE) in December 2000, July 2003 and September 2004. We downloaded the spectra from the Multimission Archive at Space Telescope (MAST) and processed them with CalFUSE v3.2.3 (Dixon et al. 2007). Given the apparent lack of variability in the Ne VIII absorption troughs located in the higher S/N part of the spectra, we combined them together in order to produce a coadded spectrum with S/N \sim [2 – 6] per resolution element ($R \sim 20000$) that covers the [920 – 1180] Å range of FUSE. Comparison of the Ne VIII troughs with the one observed with COS show no apparent changes within the lower FUSE S/N.

In addition to the troughs reported in the recent COS observations, we detect absorption associated with the high ionization Mg x λ 624.94 and O v λ 629.73 within the FUV extended FUSE range (see Figure 7). The limited S/N in the bluer range of FUSE combined with the contamination from Galactic H_2 absorption lines does not allow us to confirm the detection of the strongest Mg x λ 609.79 absorption troughs. We estimate the column density present in Mg x and O v by scaling the high S/N non-blended COS template of Ne VIII λ 770.41 and O VI λ 1031.91 to the observed residual intensities of both species in the FUSE spectra for components in region TA and TB respectively. We report the estimated column densities in Table 1 and consider them as lower limits in the remainder of the analysis.

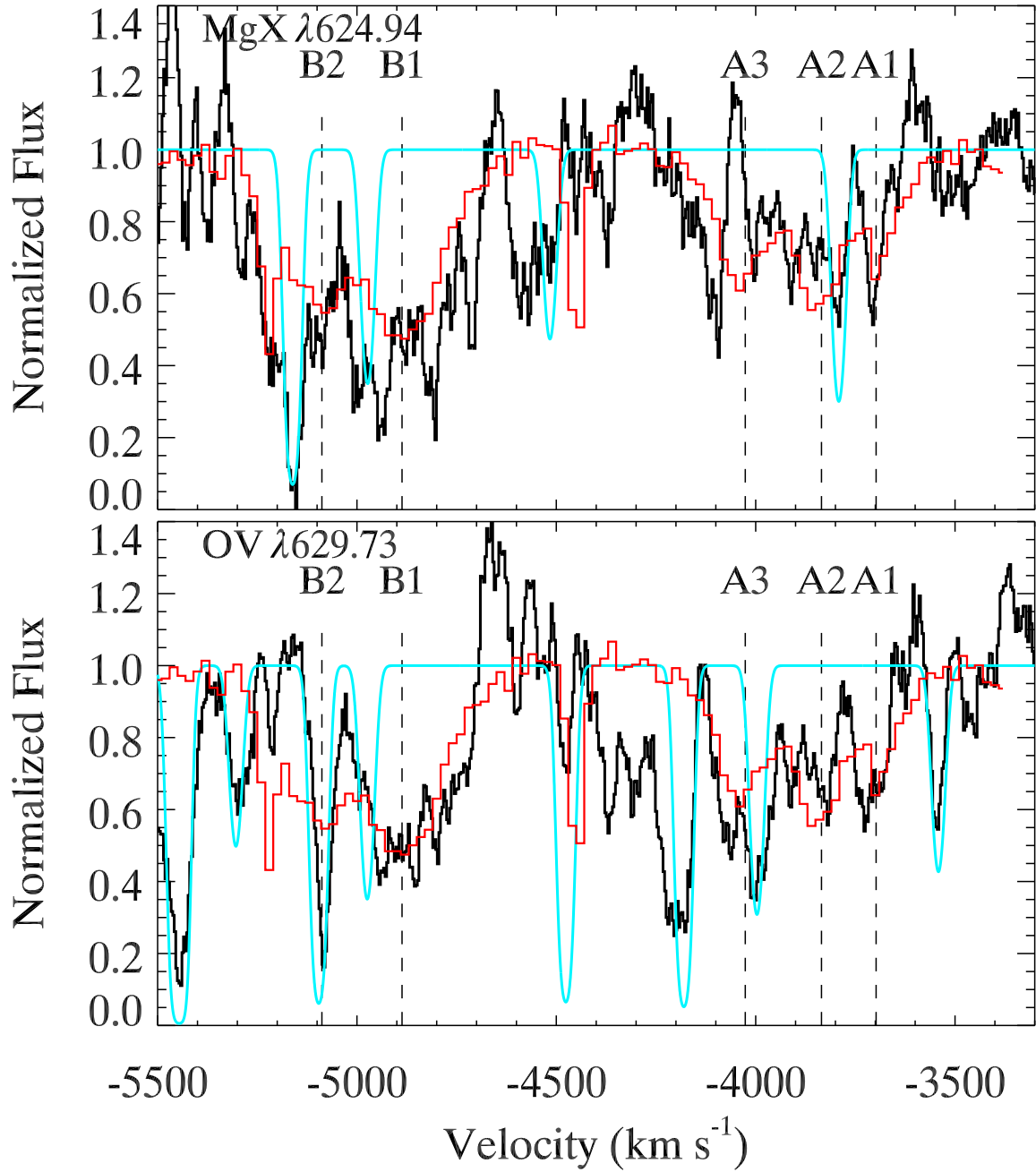


Fig. 7.— FUSE spectrum of HE0238-1904 in the O v and Mg x absorption line regions. The FUSE spectrum (in black) has been smoothed by an 8 pixel boxcar for clarity due to the limited S/N of the observations. In light blue we display an tentative Galactic H_2 absorption model considering only the first 6 J levels. In red we overplotted the Ne VIII $\lambda 780.324$ line profile, helping in the identification of the intrinsic O v and Mg x absorption features.

Table 1. COLUMN DENSITIES

Ions	v_{A3} (10^{12} cm^{-2})	v_A (10^{12} cm^{-2})	$v_A \text{ M12}^a$ (10^{12} cm^{-2})	v_B (10^{12} cm^{-2})	$v_B \text{ M12}^a$ (10^{12} cm^{-2})
H I	$\in [50.9, 183]$	$\in [92.5, 225]$	≤ 315	$\in [165, 506]$	$\in [188, 612]$
N IV	$6.82^{+1.20}_{-1.13}$	$19.9^{+2.1}_{-2.1}$	21	$12.2^{+1.5}_{-1.4}$	20
O IV	$64.2^{+6.1}_{-5.9}$	$98.7^{+8.7}_{-8.2}$	147	$34.4^{+5.7}_{-5.1}$	≤ 28
O IV *	$49.5^{+7.0}_{-6.8}$	$94.0^{+10.4}_{-9.6}$	–	$28.0^{+6.3}_{-5.8}$	–
O VI (AOD)	161^{+7}_{-7}	$> 661^{+20}_{-19}$	695	748^{+23}_{-22}	877
O VI (PC)	309^{+46}_{-28}	$> 995^{+173}_{-41}$	–	1480^{+680}_{-83}	–
O VI (PL)	543^{+118}_{-83}	$> 2980^{+910}_{-140}$	–	4500^{+1190}_{-140}	–
Ne VIII (AOD)	420^{+15}_{-14}	1790^{+30}_{-30}	1830	1990^{+20}_{-20}	2520
Ne VIII (PC)	551^{+32}_{-26}	2560^{+1480}_{-80}	–	2940^{+100}_{-80}	–
Ne VIII (PL)	830^{+74}_{-62}	5330^{+1350}_{-110}	–	6220^{+1360}_{-140}	–
C III	< 6.96	< 27.4	–	< 12.3	–
N III	< 31.7	< 125	37	< 144	≤ 97
O III	< 33.6	< 94.7	–	< 66.3	–
S VI	< 5.69	< 13.5	–	< 27.1	–
Mg X	–	> 1690	773	> 2150	1250
O V	–	> 200	64	> 170	141

a - Column densities reported in the analysis of the absorber in Muzahid et al. (2012).

6. Photoionization Analysis

The ionic column densities (N_{ion}) we measure are a result of the ionization structure of the outflowing material. These N_{ion} can be compared to photoionization models to determine the physical characteristics of the absorbing gas. Two main parameters govern the photoionization structure of each absorber: the total hydrogen column density (N_H) and the ionization parameter

$$U_H \equiv \frac{Q_H}{4\pi R^2 n_H c} \quad (5)$$

(where Q_H is the rate of hydrogen-ionizing photons emitted by the object, c is the speed of light, R is the distance from the central source to the absorber and n_H is the total hydrogen number density). We model the photoionization structure and predict the resulting ionic column densities by self-consistently solving the ionization and thermal balance equations with version c08.01 of the spectral synthesis code CLOUDY, last described in Ferland et al. (1998). We assume a plane-parallel geometry for a gas of constant n_H and initially use solar abundances and an SED tailored for this object (other SEDs and metallicities will be explored in Section 6.2). To find the pair of (U_H, N_H) , defined as a phase, that best predicts the set of observed column densities, we vary U_H and N_H in 0.1 dex steps to generate a grid of models (following the same approach described in Edmonds et al. 2011) and perform a minimization of the function

$$\chi^2 = \sum_i \left(\frac{\log(N_{i,mod}) - \log(N_{i,obs})}{\log(N_{i,obs}) - \log(N_{i,obs} \pm \sigma_i)} \right)^2 \quad (6)$$

where, for ion i , $N_{i,obs}$ and $N_{i,mod}$ are the observed and modeled column densities, respectively, and σ_i is the error in the observed column density.

6.1. Photoionization Modeling

We begin by examining models of trough A that assume solar abundances and use the SED tailored to our object (see section 6.2). In section 6.2 we relax these assumptions and explore models with different metallicities and SEDs.

The photoionization solutions for trough A are constrained by the column densities (N_{ion}) measured for H I, O IV, O V, O VI, Ne VIII and Mg X. where we use the N_{ion} reported in Table 1. For cases where doublet troughs are available we use the power-law values (PL). As we have shown in Arav et al. (2008) the PL absorber model gives a better fit in general for outflow absorption troughs than do partial covering models, and is also more physically plausible. The C III, N III, O III and S VI upper limits are already satisfied by the upper limit on H I, so they do not contribute to the χ^2 . A phase plot of the results for a grid of photoionization models for trough A is presented in Figure 8. The one-phase solution (from the χ^2 minimization) is marked with a red cross. In Figure 9 we give a graphical representation for the discrepancy between the predicted N_{ion} of this model and our measured ones (filled circles in the top panel). It is evident that the one-phase solution fit is unacceptable as the discrepancies for most N_{ion} are between 5σ and 10σ . (From the other solid points on Figure 9, we deduce that this result is rather SED independent).

The inability of one ionization phase to provide an acceptable physical model for the outflow is a major conclusion of this work and therefore we discuss its robustness. Looking at Figure 8 we observe the following: since the ratios of the oxygen ions is insensitive to changes in chemical abundances, a one-phase ionization solution would exist where the O IV and O VI curves cross in Figure 8 (this also satisfies the O V constraint as in practice, the O V N_{ion} is a lower limit). However, as can be seen from the figure, such a solution underpredicts the Ne VIII and Mg X N_{ion} by more than two orders of magnitude. In the context of a one phase model, the only way to arrive at an acceptable solution is to increase the relative abundances of neon and magnesium to oxygen by at least two orders of magnitude. This, of course, is highly implausible. In the compromise χ^2 one phase solution (red cross on Figure 8) the O IV N_{ion} is underpredicted by 10σ and the O VI N_{ion} is overpredicted by 5σ , which is unacceptable at a high confidence level

We also note that we do not use the N IV N_{ion} as a constraint because its photoionization curve on Figure 8 parallels that of O IV with a 30% lower N_H value. Such a small difference

can be eliminated by a 30% change in the N/O abundance ratio, which is well within the allowed range in theoretical abundances models (see below).

Having demonstrated that the one-phase solution is physically unacceptable, we next try a two-phase solution (e.g. Borguet et al. 2012b). Qualitatively, the first phase can be found from Figure 8, which shows that all the contours (except for O IV) overlap near $\log U_H \sim 0.5$ and $\log N_H \sim 20.5$. An ionization solution at that point would predict the observed column densities for H I, O VI, Ne VIII and Mg X, but severely under-predict O IV. Therefore, a second, low-ionization phase is required to predict the observed O IV without adding significantly to the predictions of the other ions. Such a solution would appear along the O IV contour and below the O V contour in Figure 8. The actual two-phase solution can be found by minimizing the χ^2 function given by equation (6), where $N_{i,mod}$ becomes the sum of the predicted column densities from both ionization solutions. The best two-phase solution is shown in Figure 8 as black dots at $\log U_{H,low} = -1.4^{+0.7}_{-0.1}$, $\log N_{H,low} = 17.9^{+0.8}_{-0.1}$, $\log U_{H,high} = 0.50^{+0.04}_{-0.04}$ and $\log N_{H,high} = 20.6^{+0.1}_{-0.1}$. The black dots are surrounded by contours representing the solutions with $\chi^2 = \chi^2_{min} + 1$. If $\chi^2_{min} \geq 1$, then the contours represent solutions with $\chi^2 = 2\chi^2_{min}$, which is equivalent to renormalizing to $\chi^2_{min} = 1$ and adding $\Delta\chi^2 = 1$. Note that the errors are correlated as is demonstrated graphically in Figure 8. The column density discrepancy for the two-phase solution is illustrated in the top panel of Figure 9 with open circles, and is below 1σ for each ion. It is clear that a two-phase solution fits the observations better than a one-phase solution and is an acceptable physical model. This result also holds for the model variations discussed in the next section.

6.2. Solution Dependency on Spectral Energy Distribution and Metallicity

The photoionization and thermal structure of an outflow depends on the spectral energy distribution (SED) incident upon the outflow. Traditionally the MF87 SED (Mathews & Ferland 1987) is used to model radio-loud quasars since, as Dunn et al. (2010b) explains, the samples of “typical” quasars used to construct the MF87 SED were dominated by radio-loud QSOs. Telfer et al. (2002) found, from a sample of radio-quiet quasars, a much softer continuum compared to the MF87 SED. Since HE0238-1904 is a radio-quiet quasar, the slope of the observed continuum indeed suggests a lack of the so-called big blue bump characteristic of the MF87 SED (the solid black line in Figure 10). For this reason, we developed an SED appropriate for HE0238-1904 by matching the far-UV shape to the COS data and largely mimicking the standard MF87 SED at other energies. As an added comparison, we include the UV-soft SED previously used for high luminosity, radio-quiet quasars described in Dunn et al. (2010b). These three SEDs are shown in Figure 10, and their bolometric luminosity (L_{bol}) and emission rate of hydrogen ionizing photons (Q_H) are listed in Table 2. Calculations were made using the fitted continuum model for the observed flux of the object (see Section 3.2) which gives $F_{1230} = 1.57 \times 10^{-14}$ ergs s $^{-1}$ cm $^{-2}$ Å $^{-1}$ and using a standard cosmology ($H_0 = 73.0$ km s $^{-1}$ Mpc $^{-1}$, $\Omega_\Lambda = 0.73$, and $\Omega_m = 0.27$).

Table 2. PROPERTIES OF THE CHOSEN SEDS

SED	HE0238	MF87	UVsoft
L_{bol} (10^{47} erg s $^{-1}$)	1.50	1.62	1.39
Q_H (10^{57} s $^{-1}$)	0.841	1.33	0.992

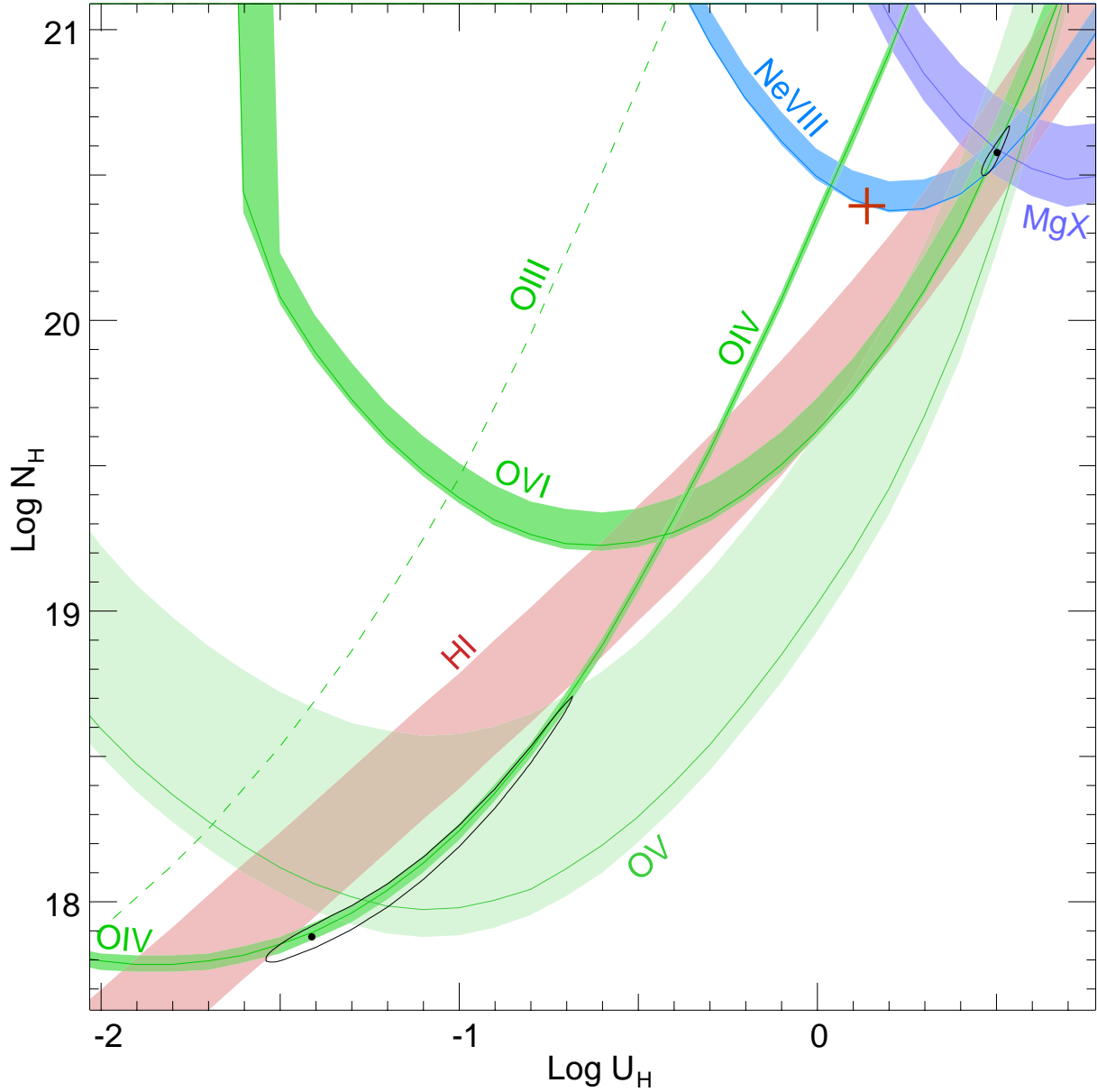


Fig. 8.— Phase Plot showing the ionization solution(s) for trough A using the HE0238 SED and assuming solar metallicity. Each colored contour represents the locus of models (U_H, N_H) which predict a column density consistent with the observed column density for that ion. The bands which span the contours are the $1-\sigma$ uncertainties in the measured observations. The dashed line indicates the O III upper limit. The red cross is the one-phase solution, while the black dots are the two-phase solutions and are surrounded by χ^2 contours (see text).

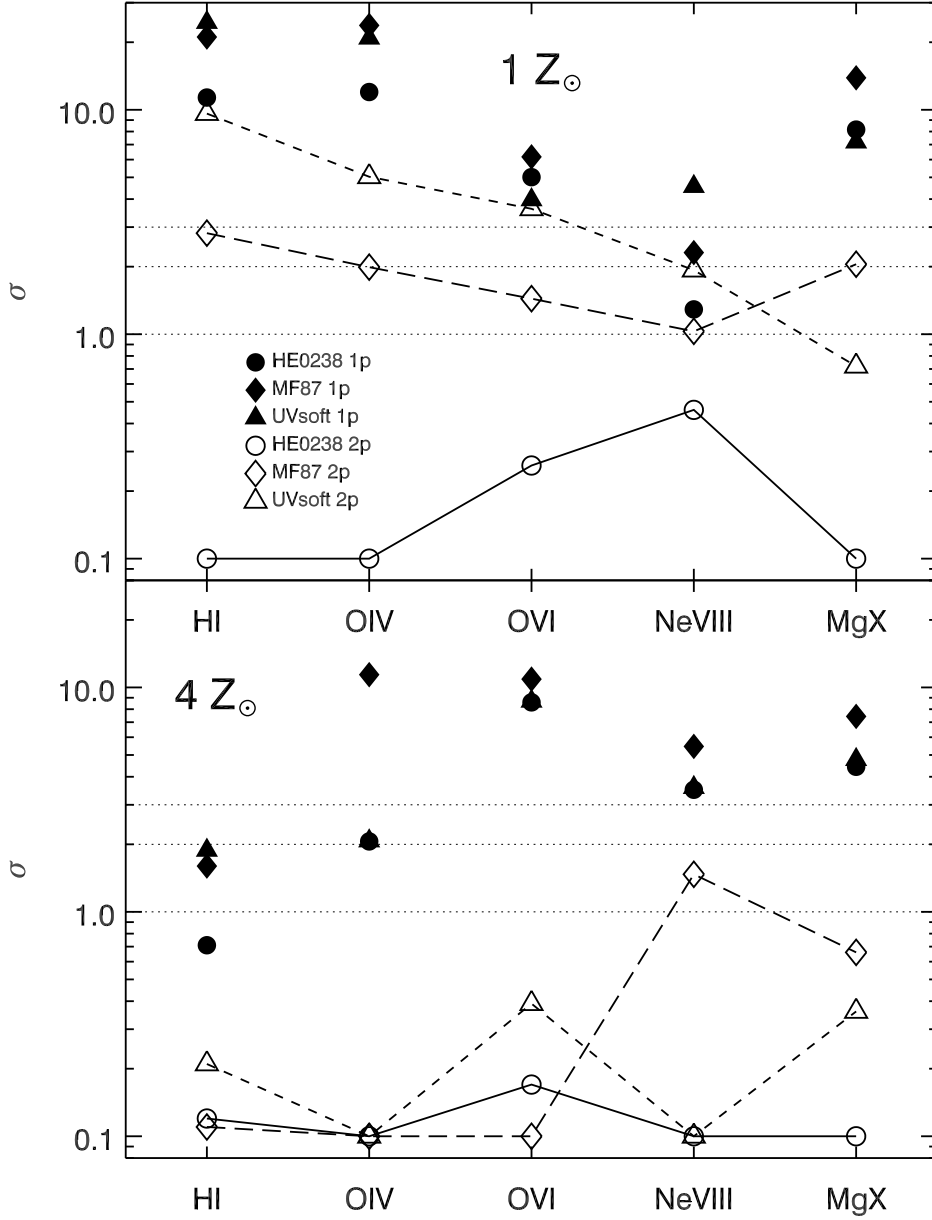


Fig. 9.— A graphic table comparing the discrepancy between the modeled and observed column densities for the one-phase and two-phases solutions for each ion. The top and bottom panels correspond to the $1Z_{\odot}$ and $4Z_{\odot}$ cases respectively, while the shape of the symbols in each panel represents the SED considered (for SED description see Table 2 and Fig. 10). The filled and open symbols show the error for the one- and two-phase solutions, respectively. The Y-axis shows the number of standard deviations from the observed column densities that each model predicts. The large discrepancy values of the one parameter solution make them physically implausible in all cases.

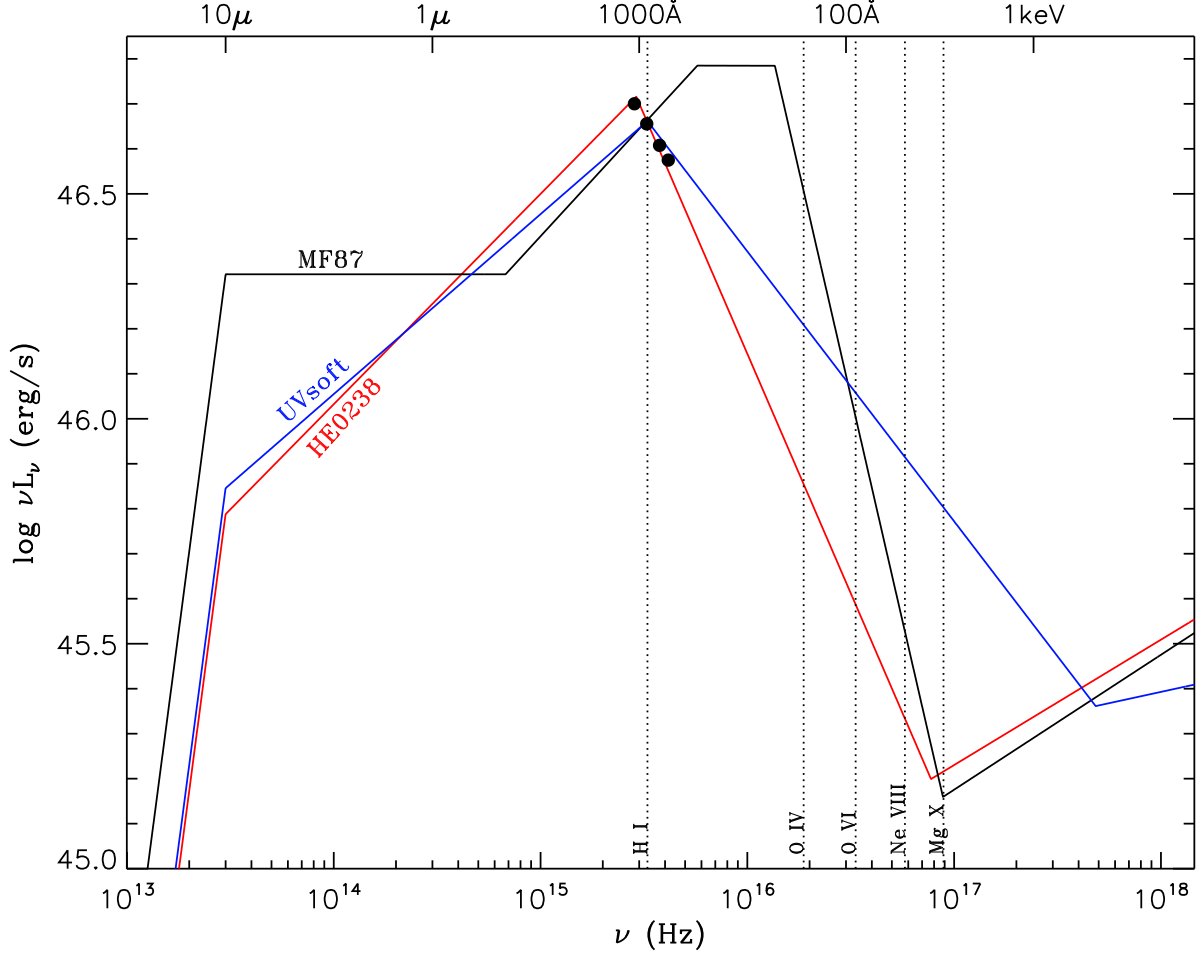


Fig. 10.— Comparison of the SEDs used in the analysis of HE0238-1904. The black dots represent the COS data used to scale the SEDs, and the dotted lines show the ionization destruction potential for some of the ions used to constrain the photoionization solution. The HE0238 SED is used as the “standard” SED for our models.

We consider the HE0238 SED the most physically plausible SED for this object, while the MF87 or UVsoft SEDs are used to demonstrate the sensitivity of the photoionization solution to other QSO SEDs used in the literature. The effect of the different SEDs can be seen in the high-ionization phase in Figure 11, where the MF87 and UVsoft SED increases and decreases the ionization parameter relative to the HE0238 SED by ~ 0.2 dex, respectively. These differences arise since the high-ionization phase is dominated by the

O VI, Ne VIII and Mg X, whose ionization destruction potentials occur in a frequency range (see Figure 10) where the three SEDs differ in power-law indices.

The other main parameter that affects the photoionization and thermal structure of an outflow is the metallicity of the gas. AGN outflows are known to have supersolar metallicities (e.g. Mrk 279: $Z \simeq 2Z_{\odot}$, Arav et al. 2007; SDSS J1512+1119: $Z_{\odot} \lesssim Z \lesssim 4Z_{\odot}$, Borguet et al. 2012a; SDSS J1106+1939: $Z = 4Z_{\odot}$, Borguet et al. 2013). We therefore consider the effects of different metallicities on the ionization solution for each SED, using the elemental abundance scaling defined for CLOUDY starburst models (which follows grid M5a of Hamann & Ferland 1993). Increase in metallicity (see Figure 11) lowers the total hydrogen column density (N_H) for both ionization phases roughly inversely linearly. This effect can be used to constrain the metallicity of the outflow by lowering the model’s metallicity until the Ne VIII contour has shifted above the H I band in Figure 8. This occurs at $Z \simeq \frac{1}{4}Z_{\odot}$ and does not allow the high-ionization phase model to fit both the H I and Ne VIII measurements, which result in a large χ^2 and make the solution physically implausible.

The upper limit on the metallicity can be found by raising the metallicity until both ionization phases cannot produce the H I N_{ion} lower limit. At this metallicity, the high-ionization phase would still have to be at the crossing of Mg X, Ne VIII and O VI. The low-ionization solution must be along the O IV contour and below the O III upper limit (If the solution is above the O III upper limit we should detect an O III trough.). Therefore, the low-ionization solution the maximizes the H I N_{ion} and does not violate other N_{ion} constraints, is found at the crossing point of the O IV measurement and the O III upper limit contours. We find that this transition occurs at $Z \simeq 4Z_{\odot}$. At higher Z values, the discrepancy between the measured H I N_{ion} and the total H I N_{ion} from both phases, leads to unaccepted large values of χ^2 . Combing the upper and lower limits on the metallicity, we obtain a possible range of $\frac{1}{4}Z_{\odot} \lesssim Z \lesssim 4Z_{\odot}$.

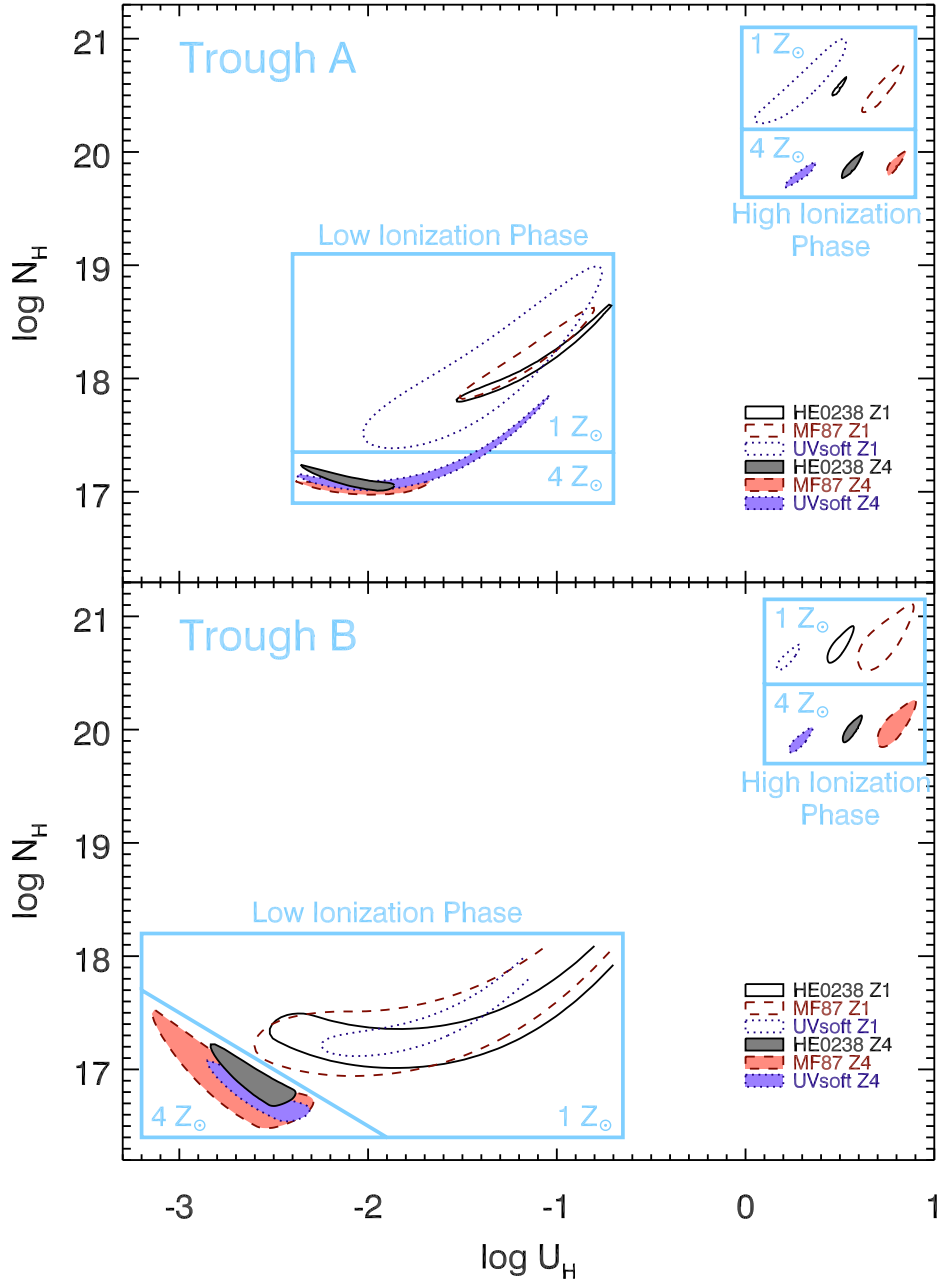


Fig. 11.— Phase Plot for the two-phase ionization solutions for the 2 troughs, 3 SEDs and 2 metallicities for a total of 12 models. All the models agree on the existence of a two-phase outflow. The χ^2 contour for the low-ionization phase of the $1Z_\odot$ models for trough B can continue up to $\log N_H \sim 19.7$ and $\log U_H \sim -0.4$ (see text). Increasing the metallicity from $1Z_\odot$ to $4Z_\odot$ lowers the hydrogen column density of both components roughly inversely linearly. The SED shape only affects the high-ionization component by shifting its ionization parameter by ~ 0.2 dex in either direction compared to the standard HE0238 SED.

Trough B at $\sim -5000 \text{ km s}^{-1}$ is kinematically separated from trough A ($\sim -3850 \text{ km s}^{-1}$), as both have $\Delta v \sim 500 \text{ km s}^{-1}$ (see Figure 5). However, we find that these two troughs have strong resemblance in their physical characteristics. Both have similar photoionization solutions, as is evident by the two panels of Figure 11. For the SEDs and metallicities considered, both troughs show clear evidence for the existence of a two ionization-phase outflow separated by $\Delta U_H \sim 2\text{dex}$ and $\Delta N_H \sim 2.5\text{dex}$. They also have indistinguishable number density for their low ionization phase (see next section).

For the solar metallicity case, the low ionization solution for trough B can be anywhere along the O IV contour up to $\log N_H \sim 19.7$ and $\log U_H \sim 0.0$ (extending the χ^2 contour shown in Figure 11, for the $1Z_\odot$ cases). The reason for this behavior is that for $1Z_\odot$ all the other N_{ion} are well predicted by the high-ionization phase, including H I. Therefore, any position along the O IV contour, which is well below the H I band will yield the desired $N(\text{O IV})$, while contributing negligibly to the other predicted N_{ion} . For higher metallicity, the high-ionization phase cannot produce enough $N(\text{H I})$, therefore most of the H I must come from the low ionization phase, which cause it to place the solution close to the crossing point of the O IV contour and H I band. We note that in all these cases a lower ionization phase is necessary to produce not only the observed O IV but also the observed N IV. Using the same methods from trough A, we obtain a possible range of $\frac{1}{4}Z_\odot \lesssim Z \lesssim 3Z_\odot$.

6.3. Comparison With the Results of Muzahid et al. (2012)

Muzahid et al. (2012, hereafter M2012) analyzed the same observations of HE0238-1904. We compare their ionic column density (N_{ion}) measurements to ours in Table 1. Most of the measurements agree to better than a factor of two (particular good agreement for the AOD measurements of the deepest COS troughs: O VI and Ne VIII). However, as expected, our power-law measurements are consistently larger by roughly a factor of 3.

M2012 found that the outflowing material cannot be in one ionization phase; a major

finding that we concur with. A quantitative comparison between our results and those reported by M2012 is complicated due to the different approaches both groups have taken in the analysis. M2012 photoionization analysis concentrated on finding U_H values that reproduced individual ratios of N_{ion} measurements for each of their 5 labeled components (see their Figure 4 and accompanying text). Our approach, as detailed above, is to find a full two-phase photoionization model that simultaneously accounts for all the measured N_{ion} , in each of the troughs A and B. With these differences in mind, we note that for the high ionization phase, M2012 obtains $0.8 < \log U_H < 1.2$ for components 3, 4 and 5 (covering the bulk of both A and B troughs), less than a factor of 3 difference from our results of $0.2 < \log U_H < 0.8$ (see Fig. 11). The low ionization phase is less constrained in M2012, as they only use comparison of high ionization to low ionization N_{ion} (i.e., O VI/O IV and O VI/N IV). It is thus not surprising that our U_H for the low ionization phase are roughly two orders of magnitude lower than the constraints achieved from the O VI/O IV and O VI/N IV ratios. We cannot compare N_H values as they are not reported by M2012.

7. ENERGETICS

We use equation set (1) to estimate the mass flow rate and kinetic luminosity of the outflow. As described in section 2, to do so we need to measure or constrain the values for N_H , R and Ω . The first of these (N_H) was determined by fitting the N_{ion} measured in section 4 with the prediction from a grid of CLOUDY simulations (see previous section). The ionization parameter U_H was determined simultaneously with N_H , and will be used in section 7.1 to determine the distance between the absorber and the central source. Constraints on global covering fraction Ω are elaborated on in section 7.2. Following these preliminary steps we derive and discuss the energetics of the outflow components (Section 7.3 and Table 3)

7.1. Determining the Number Density and Distance of the Outflow

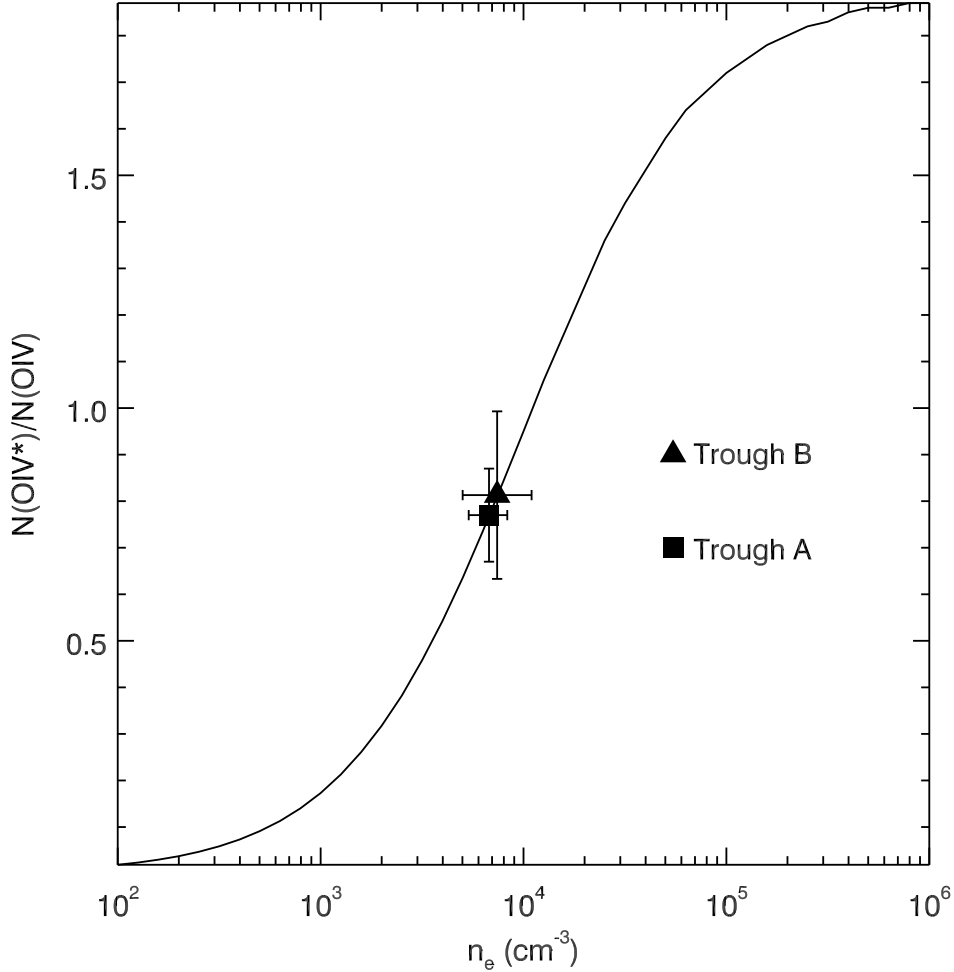


Fig. 12.— Density diagnostic for HE0238-1904 trough A and B. We overlay their measured $N_{ion}(\text{OIV}^*)/N_{ion}(\text{OIV})$ on the theoretical level population assuming a temperature of 10^4K , to obtain the electron number densities (n_e) inferred from the collisional excitation model. The n_e is translated to n_H via the relation $n_e \simeq 1.2n_H$, valid for highly ionized plasma.

In highly ionized plasma the hydrogen number density is related to the electron number density through $n_e \simeq 1.2n_H$. To determine n_e for trough A we use the measured the $N_{ion}(\text{OIV}^*)/N_{ion}(\text{OIV})$ ratio in trough A3 (the portion of trough A where the excited state

appears) and similarly for trough B. Figure 12 shows the observed ratios between O IV* and O IV plotted on the theoretical dependence of this ratio on n_e , for both troughs. The error on the observed column densities translates into errors on the n_e , yielding a measurement of $\log(n_H) = 3.75 \pm 0.10 \text{ cm}^{-3}$ for trough A and $\log(n_H) = 3.79 \pm 0.17 \text{ cm}^{-3}$ for trough B. We note that both troughs have the same number density within the measurement error.

The $N_{ion}(\text{O IV}^*)/N_{ion}(\text{O IV})$ ratio was derived using a sub portion of each trough. Therefore, we need to address the physical relationship between these sub-components and the more extended troughs. The kinematic correspondence, suggests a co-spatial location for the gas that shows O IV* and O IV with the full parent trough. We can further solidify this connection by comparing the overall photoionization solution of each subtrough to its parent trough. We find that there is a very good agreement in both cases. For example: The photoionization solution for trough A3 is virtually identical to that of trough A, as the ionization parameters for both the high and low ionization phases differ by only ~ 0.1 dex. This strong physical resemblance combined with the kinematic correspondence solidifies the case that trough A3 is indeed a physical portion of outflow component A. A similar situation exists for trough B.

We determine R for each component by substituting the measured n_H combined with the U_H of each low ionization phase (where all the O IV gas resides), and the Q_H given in table 2 into equation (5). The results for all cases are shown in Table 3.

7.2. Constraining Ω

For a full discussion about constraining Ω that is needed for equation set (1), we refer the reader to Section 5.2 in Dunn et al. (2010b). Here we reproduce the main arguments and then concentrate on the case of Ne VIII outflows. There is no direct way to obtain the Ω of a given outflow from its spectrum as we only see the material located along the line of sight. Therefore, the common procedure is to use the fraction of quasars that show outflows

as a proxy for Ω .

A significant amount of work was directed towards finding the frequency of detecting different categories of quasar outflows from the full population of quasars (Hewett & Foltz 2003; Ganguly & Brotherton 2008; Dai et al. 2008; Knigge et al. 2008; Dunn et al. 2012; Dai et al. 2012). However, none of these studies addressed the frequency of quasar outflows that show troughs from Ne VIII, the highest abundant ionization species seen in the UV. Recently, this issue was addressed by Muzahid et al. (2013) who found 11 Ne VIII outflows in 20 quasar spectra. The width of these outflow troughs is mainly between 200–700 km s⁻¹, straddling the ~ 450 km s⁻¹ width we measure for troughs A and B in HE 0238 – 1904. We therefore use $\Omega = 0.5$ as a representative for this class of outflows.

7.3. Results

For the analysis of the 2 observed troughs, we have considered 3 different SEDs combined with 2 possible metallicities for a total of 12 model variations. In Table 3 we detail the main results for each model. The 1st column designates the SED used; the 2nd column gives the $\log(U_H)$ of the low-ionization phase, since this is the U_H that determines the distance of the absorber (see section 7.1); column 3 gives the $\log(N_H)$ of the high-ionization phase, as it carries the vast majority of outflowing column density; in the 4th column we provide the distance of the outflow component using the U_H reported in the 2nd column and the calculation detailed in section 7.1; the 5th through 7th columns give the mass flow rate, kinetic luminosity and its percentage from the total L_{Bol} of the quasar, by substituting N_H and R from columns 3 and 4 into equation set (1), and using $\Omega = 0.5$ (see section 7.2)

The results of these models can be summarized as follows:

1. *Trough A vs Trough B:* trough B carries roughly 5 times more kinetic luminosity than trough A. This is due to its 30% greater velocity, 70% higher R and a 25% larger N_H .
2. *Solar vs Supersolar Metallicity:* the higher metallicity models result in a lower N_H by a

factor roughly inversely linear with the metallicity. For trough A, the ionization parameter for the low-phase also decreases, suggesting that the outflow could be twice as far from the central source if a higher metallicity is assumed. These combined effects result in a kinetic luminosity 3 times lower than that of solar metallicity models.

3. SED dependence: The energetics are rather insensitive to the SED shape. The ionization parameter of the high-phase changes by up to a factor of 4, but the N_H is unaffected. For the low-ionization phase the differences in U_H are all within the allowed χ^2 contours: no apparent trend is detected.

We emphasize that the HE0238 SED we use is the most appropriate given the spectral data on hand. In addition, the $Z = 4Z_\odot$ case gives a slightly better fit to the measured column densities than the pure solar case. At the same time, it provides a more conservative (lower) estimate for the kinetic luminosity of this outflow. We therefore use this model as the representative result for the outflow.

For the two separate outflow components of HE0238-1904 (troughs A and B), we select trough B as the representative of the energetics contained within this object, since trough B has roughly 5 times more energy than trough A. We show this result in Table 4 along with the results from our previous \dot{E}_k record holders: SDSS J1106+1939 (Borguet et al. 2013) and SDSS J0838+2955 (Moe et al. 2009, but see the correction by a factor of 0.5 reported in Edmonds et al. 2011).

Table 3. MODEL COMPARISON

SED	$\log(U_H)$	$\log(N_H)$ (cm^{-2})	R (kpc)	\dot{M} ($M_\odot \text{yr}^{-1}$)	\dot{E}_k ($10^{45} \text{ erg s}^{-1}$)	\dot{E}_k/L_{Bol} (%)
Trough A ($v = -3850 \text{ km s}^{-1}$)						
Z = 1Z$_\odot$						
HE0238	$-1.4^{+0.7}_{-0.1}$	$20.6^{+0.09}_{-0.09}$	$1^{+0.29}_{-0.57}$	27^{+10}_{-15}	$0.522^{+0.2}_{-0.3}$	$0.35^{+0.1}_{-0.2}$
MF87	$-1.1^{+0.3}_{-0.4}$	$20.5^{+0.2}_{-0.2}$	$0.91^{+0.61}_{-0.28}$	22^{+25}_{-10}	$0.43^{+0.5}_{-0.2}$	$0.27^{+0.3}_{-0.1}$
UVsoft	$-1.3^{+0.5}_{-0.7}$	$20.5^{+0.5}_{-0.3}$	$0.99^{+1.3}_{-0.47}$	23^{+70}_{-14}	$0.452^{+1}_{-0.3}$	$0.32^{+0.9}_{-0.2}$
Z = 4Z$_\odot$						
HE0238	$-2^{+0.1}_{-0.4}$	$19.8^{+0.2}_{-0.06}$	$2^{+1.2}_{-0.32}$	9.3^{+8}_{-2}	$0.179^{+0.1}_{-0.04}$	$0.12^{+0.1}_{-0.02}$
MF87	$-1.9^{+0.2}_{-0.5}$	$19.9^{+0.1}_{-0.09}$	$2.2^{+1.9}_{-0.49}$	11^{+11}_{-3}	$0.22^{+0.2}_{-0.06}$	$0.14^{+0.1}_{-0.04}$
UVsoft	$-1.8^{+0.8}_{-0.6}$	$19.8^{+0.2}_{-0.07}$	$1.8^{+1.8}_{-1}$	6.9^{+8}_{-4}	$0.133^{+0.2}_{-0.08}$	$0.096^{+0.1}_{-0.06}$
Trough B ($v = -5000 \text{ km s}^{-1}$)						
Z = 1Z$_\odot$						
HE0238	$-2.4^{+2}_{-0.1}$	$20.8^{+0.1}_{-0.2}$	$3^{+0.88}_{-2.8}$	160^{+80}_{-150}	5.32^{+3}_{-5}	$3.5^{+1.7}_{-3}$
MF87	$-2.2^{+2}_{-0.3}$	$20.9^{+0.2}_{-0.4}$	$3.1^{+1.7}_{-2.8}$	210^{+200}_{-200}	6.86^{+7}_{-6}	4.2^{+4}_{-4}
UVsoft	$-1.8^{+1}_{-0.4}$	$20.7^{+0.09}_{-0.1}$	$1.7^{+1.2}_{-1.2}$	69^{+50}_{-50}	$2.25^{+1.8}_{-1.7}$	$1.6^{+1.3}_{-1.2}$
Z = 4Z$_\odot$						
HE0238	$-2.5^{+0.09}_{-0.4}$	$20^{+0.1}_{-0.1}$	$3.4^{+2}_{-0.49}$	31^{+20}_{-9}	$1^{+0.7}_{-0.3}$	$0.67^{+0.5}_{-0.2}$
MF87	$-2.5^{+0.2}_{-0.7}$	$20^{+0.2}_{-0.2}$	$4.2^{+5.2}_{-0.86}$	40^{+60}_{-15}	$1.29^{+2}_{-0.5}$	$0.8^{+1.3}_{-0.3}$
UVsoft	$-2.4^{+0.1}_{-0.4}$	$19.9^{+0.1}_{-0.1}$	$3.4^{+2.5}_{-0.51}$	24^{+20}_{-6}	$0.772^{+0.7}_{-0.2}$	$0.56^{+0.5}_{-0.13}$

8. A TWO PHASE OUTFLOW

One of the important findings of this paper is the existence of at least two widely different ionization phases in the outflow. For both outflow components we find that the two phases differ by roughly 2.5–3 orders of magnitude in U_H and similarly in N_H (where the higher ionization phase has the larger N_H). The robustness of this result relies on: a) the inability of a single phase solution to produce a reasonable fit for the measured N_{ion} , b) an excellent fit achieved by the two-phase models, c) reliable N_{ion} extractions, and d) a need for a two-phase solution that is independent of the assumed SED or metallicity. In addition, the high spectral resolution of the data plus the ionization modeling of the different sub-components give high confidence to the assertion that the two phases are co-spatial in both components.

8.1. Geometry and Filling Factor

An interesting physical picture of the outflow emerges from the two-phase solution. For component B (using our standard HE0238 SED and $4Z_\odot$ metallicity) we find that the high-ionization phase (hereafter phase 2) carries a thousand times more column density than the low-ionization phase (hereafter phase 1). At the same time the two phases differ in U_H by a similar factor. Therefore, phase 1 is inferred to have a volume filling factor of $\sim 10^{-6}$ embedded within a much more massive and extended phase 2. We also determined that in the hot phase $\log(n_H) = 0.8 \text{ cm}^{-3}$ (from our determination of n_H for the phase 1 and their difference in U_H) and $N_H \sim 10^{20} \text{ cm}^{-2}$. Therefore, the thickness of this outflow is $\Delta R = N_H/n_H \simeq 5pc$. As we show in section 8.3, x-ray observations of the NGC 3783 outflow show an even higher ionization phase to which the UV data of HE0238-1904 is not sensitive. If a similar phase exists in the HE0238-1904 outflows then the full width of the outflow will be $\Delta R \simeq 70pc$ (see section 8.3).

8.2. Are the Two Phases in Pressure Equilibrium?

For component A (using our standard HE0238 SED and $4Z_{\odot}$ metallicity) our CLOUDY models, which assume only photoionization equilibrium, give a temperature of $7 \times 10^3 K$ and $7 \times 10^4 K$ for phase 1 and 2, respectively. Such a situation is far from pressure equilibrium between the two phases, since the factor 10 higher temperature cannot compensate for the factor of 300 lower density of phase 2 compared to phase 1 (inferred from the difference in their U_H). Therefore, if the ionization equilibrium and thermal balance of the outflow are caused only by photoionization, the two phases cannot be in pressure equilibrium. This will make the phase 1 material unstable on roughly its dynamical time-scale for expansion: $t = D/v_{th} \lesssim [N_H/n_H]/v_{th} \simeq [10^{17}/10^4]/10^6 \simeq 10^7$ seconds, which is less than a year (where D , N_H , n_H and v_{th} are the maximum size, column density, number density and thermal velocity of the low-ionization absorber, respectively).

However, there are at least 3 mechanisms suggested in the literature that can potentially put the two phases in pressure equilibrium: a) magnetic confinement of the outflow (de Kool & Begelman 1995) b) cloudlets compressed by hot post-shock gas (Faucher-Giguère et al. 2012); and c) thermal pressure equilibrium with the high ionization phase, whose temperature is much higher than the photoionization equilibrium indicates (presumably from shock heating).

We did some preliminary tests of the last hypothesis (c) and found the following. Having the two phases in pressure equilibrium is equivalent to the requirement that $T_2 = T_1(U_{H2}/U_{H1})$ where the subscript 1 and 2 refers to the low-ionization and high-ionization-phase, respectively. CLOUDY models give us T_1 , and the number density of this phase (n_1) is known from the $N_{ion}(O\text{IV}^*)/N_{ion}(O\text{IV})$ ratio. From the definition of U_H we then obtain $n_2 = n_1(U_{H1}/U_{H2})$. We therefore proceed by running a CLOUDY model where $U_H = U_{H2}$, $n_H = n_2$ while forcing $T = T_2$. For component A we find that collisional ionization at T_2 (a few 10^6 K) causes the ionic fraction of O VI, Ne VIII and Mg X to drop by 3.3, 2.8 and 1.8 dex, respectively, compared to the pure photoionization equilibrium of

phase 2. Such reduction in ionic populations with the same N_H will not allow for enough N_{ion} to detect any troughs from these species. Simply increasing the N_H of phase 2 by two or three orders of magnitude would also not work as we either under-predict O VI or over-predict Ne VIII and Mg X.

One possible way for this mechanism to work and still yield the required N_{ion} for phase 2 is as follows. Figure 8 shows that an acceptable solution for phase 1 can be found along the O VI contour, up to $\log(U_H) = -0.7$. If we move the solution farther to the crossing point of the O IV and O VI contours [$\log(U_H) = -0.4, \log(N_H) = 19.2$], phase 1 produces all the observed O VI N_{ion} by construction. We now allow phase 2 to have a temperature high enough to be in pressure equilibrium with phase 1 ($T_2 = 2.8 \times 10^5$ K, calculated from the ΔU_H between the phases), and increase its total N_H by 0.4 dex. For this model we find that the N_{ion} for Ne VIII matches the observations exactly and that of Mg X is 0.5 dex above the measurements, which is an acceptable solution (see table 1). At this temperature and density, collisional ionization decreased the fraction of Ne VIII by 0.4 dex and increased that of Mg X by 0.1 dex. The fraction of O VI in phase 2 dropped by 1.0 dex, however, and we now obtain all the observed O VI N_{ion} from phase 1. To summarize, using the following assumptions: a heating mechanism that increases the temperature of phase 2 by roughly a factor of 3 above what a pure ionization equilibrium yields, increases the total N_H of phase 2 by 0.4 dex, and moves the solution of phase 1 to the crossing point of the O VI and O VI contours; we can obtain an acceptable solution for all the observed N_{ion} while keeping both phases in pressure equilibrium. Such a solution will put the outflow closer to the central source by a factor of three (from the difference in U_{H1}), but will not change the overall mass flux and kinetic luminosity significantly since the N_H of phase 2 will increase by a similar factor. However, the filling factor for phase 1 (see section 8.1) will increase from $\sim 10^{-5}$ to $\sim 10^{-3}$.

8.3. Comparison With Other AGN Outflows

The ionization species which yield outflow troughs in most UV AGN spectra cover a narrow range in ionization potential (IP), usually from Si IV (45 eV) to N V (98 eV) and sometimes O VI (138 eV). This small range allows for a good fit of the measurements with a single ionization phase (e.g., Edmonds et al. 2011). With coverage of the far UV we can observe Ne VIII (239 eV) and Mg X (368 eV). The larger range in IP can indicate that at least a two-phase medium is needed. We find only one case in the literature where data of Ne VIII was shown to suggest a two-phase solution (PG 0946+301, Arav et al. 2001b), with the low-ionization phase at $-2 < \log(U_H) < -1.5$ and the high ionization phase at $\log(U_H) \sim 0.5$ (deduced from their figure 7). These values are similar to those we find in HE0238-1904.

X-ray observations of Seyfert outflows, the so-called “warm absorbers”, routinely show the need for two or more ionization phases (e.g., Netzer et al. 2003; Steenbrugge et al. 2005; Holczer et al. 2007). This is mainly due to the much larger spread in IP of the observed ionic species [(e.g., O V (IP=114 eV) to O VIII (IP=871 eV)]. However, in almost all cases, the x-ray spectra lack the resolution to kinematically associate the warm absorber with the UV absorber seen in the same object. Two comprehensive analyses of the UV and X-ray photoionization equilibrium of outflows from the same object exist in the literature. For Mrk 279, Costantini et al. (2007) and Arav et al. (2007) show a remarkable agreement for the properties of the low-ionization phase of the outflow: $\log(U_H) = -1, \log(N_H) = 20$ (cm^{-2}). This is strong evidence that the two absorbers are one and the same. The X-ray data also reveals a high-ionization phase at $\log(U_H) = 1$, which makes the separation in N_H between the two phases similar to the one we see in HE0238-1904. In NGC 3783 Gabel et al. (2005a) find a single ionization solution for each of four UV outflow components spreading over $-1.6 < \log(U_H) < -0.5$ and 3 ionization phases for the warm absorber with $-0.5 < \log(U_H) < 1.3$.

The highest ionization phase detected in NGC 3783 ($\log(U_H) = 1.3$) is inferred

from troughs of the highly ionized species Si xiv (IP=2670 eV) and S xvi (IP=3500 eV). Netzer et al. (2003) find this phase to have $\log(U_H)$ 0.8 dex higher and $\log(U_H)$ 0.3 dex higher than the medium ionization phase that can be detected using Ne VIII and Mg X measurements. If a similar situation occurs in HE0238-1904 the total mass flux and kinetic luminosity of the outflowing components (A and B) will increase by a factor of 3 and the full width of the outflow will increase by 1.1 dex, and the filling factor of the low-ionization phase will drop accordingly.

Finally, we note the curious coincidence where for both outflow components in HE0238-1904, the two ionization phases fall along the H I contour on the $N_H : U_H$ plot (see Figure 8), or equivalently, have roughly a constant ratio of N_H/U_H . This situation arises mainly due to the small measured N_{ion} for O IV (and N IV), contrasted with the much larger values (20-100 times, see table 1) for Ne VIII and Mg X. A priori, our data is sensitive to a few percent of the measured Ne VIII N_{ion} . Therefore, in principle such smaller measurements would have lowered the N_H of the phase 2 by a similar amount, and thus the inferred situation is not a selection effect.

9. DISCUSSION

Significant AGN feedback processes typically require a mechanical energy input of roughly 0.5–5% of the Eddington luminosity of the quasar (Hopkins & Elvis 2010; Scannapieco & Oh 2004, respectively). HE0238–1904, being among the brightest at its redshift band radiates close to its Eddington limit (i.e. $L_{Bol} \simeq L_{edd}$). Therefore, with $\dot{E}_k \gtrsim 0.7\%L_{Bol}$, its outflow can contribute significantly to the theoretically invoked AGN feedback processes.

Prior to the work described here, our group have shown that \dot{E}_k of outflows in low-ionization BALQSO outflows are significant in the context of AGN feedback (Moe et al. 2009; Dunn et al. 2010b); as well as for the ubiquitous high ionization BALQSO

(Borguet et al. 2013). This investigation gives the first reliable estimates of R , \dot{M} and \dot{E}_k for the very high-ionization, high-luminosity quasar outflows. Cumulatively, these investigations suggest that UV absorption outflows observed in the rest-frame UV of luminous quasars, have enough kinetic luminosity to drive AGN feedback processes. In Table 4 we give the data for 3 representative types of quasar outflow: trough B in HE0238-1904 from this analysis; the high ionization outflow in SDSS J1106+1939 from Borguet et al. (2013); and the low-ionization outflow in SDSS J0838+2955 from Moe et al. (2009).

Other works have shown high mass flux (\dot{M}) for molecular outflows in luminous quasars. For example, Maiolino et al. (2012) shows such a large scale (~ 16 kpc) outflow at the very high redshift ($z=6.4189$) quasar J1148+5251. The outflow is reported to have $\dot{M} > 3500M_\odot \text{ yr}^{-1}$, but in order to have a fair comparison with \dot{M} values we give in Table 4, we need to use our \dot{M} prescription (see eq. 1) on the mass estimate from Maiolino et al. (2012) (their eq. 2) which yields a third of the original \dot{M} estimate (i.e., $\sim 1200M_\odot \text{ yr}^{-1}$).

The distances found for the two outflows we report here are a few kiloparsecs from the central source. These are similar to the distances inferred for outflows in which the density diagnostic is obtained from the study of excited troughs of singly ionized species as Fe II or Si II (e.g. Korista et al. 2008; Moe et al. 2009; Dunn et al. 2010b), but they are 4+ orders of magnitude farther away than the assumed acceleration region (0.03–0.1 pc) of line driven winds in quasars (e.g. Murray et al. 1995; Proga et al. 2000). This result is consistent with almost all the distances reported for AGN outflows in the literature. Our current investigation, expands this claim to very high ionization outflows as well. We conclude that most AGN outflows are observed very far from their initial assumed acceleration region.

Table 4. PHYSICAL PROPERTIES OF THE S IV QUASAR OUTFLOWS.

Object	$\log(L_{Bol})$ (ergs s ⁻¹)	v (km s ⁻¹)	$\log(U_H)$	$\log(N_H)$ (cm ⁻²)	$\log(n_e)$ (cm ⁻³)	R (kpc)	\dot{M} (M _⊙ yr ⁻¹)	$\log(\dot{E}_k)$ (ergs s ⁻¹)	\dot{E}_k/L_{Bol} (%)
HE0238-1904 B 4Z _⊙	47.2	-5000	-2.5 ^{+0.1} _{-0.4}	20 ^{+0.1} _{-0.1}	3.75 ^{+0.10} _{-0.10}	3.4 ⁺² _{-0.49}	31 ⁺²⁰ ₋₉	45 ^{+0.2} _{-0.2}	0.7 ^{+0.5} _{-0.2}
SDSS J1106+1939 4Z _⊙	47.2	-8250	-0.5 ^{+0.3} _{-0.2}	22.1 ^{+0.3} _{-0.1}	4.1 ^{+0.02} _{-0.37}	0.32 ^{+0.20} _{-0.10}	390 ⁺³⁰⁰ ₋₁₀	46.0 ^{+0.3} _{-0.1}	5 ⁺⁴ _{-0.3}
SDSS J0838+2955	47.5	-5000	-2.0 ^{+0.2} _{-0.2}	20.8 ^{+0.3} _{-0.3}	3.8	3.3 ^{+1.5} _{-1.0}	300 ⁺²¹⁰ ₋₁₂₀	45.4 ^{+0.2} _{-0.2}	0.8 ^{+0.5} _{-0.3}

10. SUMMARY

In this paper we first explain the immense diagnostic power of spectra at rest-frame 500\AA – 1000\AA , for quasar outflows science (see section 2 and Fig. 1), which includes:

- a) Sensitivity to the warm absorber phase of the outflow: from observing Ne VIII, Mg X and Si XII troughs.
- b) Determining the distance from the AGN for the majority of high-ionization outflows, by observing resonance and metastable troughs from such species (e.g., O IV, O V, Ne V, Ne VI)
- c) Separating abundances and photoionization effects: by measuring troughs of several ions from the same element (e.g., O II, O III, O IV, O V).

The Cosmic Origins Spectrograph (COS) onboard HST allows us to realize this powerful diagnostic potential. We can now obtain high enough quality data on bright medium-redshift quasars ($1.5 \gtrsim z \gtrsim 0.5$), yielding detailed and reliable analysis of quasar-outflows spectra in this rest-wavelength regime. We demonstrate this potential by analyzing HST/COS (and FUSE) data of the outflow seen in quasar HE 0238–1904. In the available data at rest-frame 600\AA – 1100\AA we identify and measure a small subset of these diagnostic troughs, which yielded the following important results:

1. Distance of the outflow from the AGN: measuring the column densities (N_{ion}) of O IV/O IV* $\lambda\lambda 787.711, 790.199$, yielded a distance of ~ 3000 pc. for the outflow from the AGN. This is only the second time in the literature where a distance was determined for the majority of high ionization quasar outflows (the first determination was also done by our group, see Borguet et al. 2013 and table 4 here).

2. Two co-spatial ionization phases: We measure N_{ion} of troughs from the very high ionization species Ne VIII and Mg X, as well as from the lower ionization species O IV, O V, O VI, N IV, and H I. To reproduce all of these N_{ion} , photoionization modelling require two ionization phases in the outflow, with ionization parameters separated by roughly a factor of 100 between the two phases. The low ionization phase is inferred to have a volume filling factor of $10^{-5} - 10^{-6}$.

3. Mass flux and kinetic luminosity of the outflow: the two findings above, allow us to determine robust values for the : $40 M_{\odot} \text{ yr}^{-1}$ and $10^{45} \text{ ergs s}^{-1}$, respectively, where the latter is roughly equal to 1% of the bolometric luminosity. Such a large kinetic luminosity and mass flux measured in a typical high ionization wind, suggest that quasar outflows are a major contributor to AGN feedback mechanisms.

ACKNOWLEDGMENTS

We acknowledge support from NASA STScI grants GO 11686 and GO 12022 as well as NSF grant AST 0837880. We thank Sowgat Muzahid for helpful suggestions on this manuscript.

REFERENCES

- Aoki, K., Oyabu, S., Dunn, J. P., Arav, N., Edmonds, D., Korista, K. T., Matsuhara, H., & Toba, Y. 2011, PASJ, 63, 457
- Arav, N. 1997, in *Astronomical Society of the Pacific Conference Series*, Vol. 128, *Mass Ejection from Active Galactic Nuclei*, ed. N. Arav, I. Shlosman, & R. J. Weymann, 208
- Arav, N., Becker, R. H., Laurent-Muehleisen, S. A., Gregg, M. D., White, R. L., Brotherton, M. S., & de Kool, M. 1999a, ApJ, 524, 566
- Arav, N., Brotherton, M. S., Becker, R. H., Gregg, M. D., White, R. L., Price, T., & Hack, W. 2001a, ApJ, 546, 140
- Arav, N., Kaastra, J., Kriss, G. A., Korista, K. T., Gabel, J., & Proga, D. 2005, ApJ, 620, 665
- Arav, N., Kaastra, J., Steenbrugge, K., Brinkman, B., Edelson, R., Korista, K. T., & de Kool, M. 2003, ApJ, 590, 174
- Arav, N., Korista, K. T., & de Kool, M. 2002, ApJ, 566, 699
- Arav, N., Korista, K. T., de Kool, M., Junkkarinen, V. T., & Begelman, M. C. 1999b, ApJ, 516, 27
- Arav, N., Moe, M., Costantini, E., Korista, K. T., Benn, C., & Ellison, S. 2008, ApJ, 681, 954
- Arav, N., et al. 2001b, ApJ, 561, 118
- . 2007, ApJ, 658, 829
- . 2012, A&A, 544, A33

- Barlow, T. A., Hamann, F., & Sargent, W. L. W. 1997, in *Astronomical Society of the Pacific Conference Series*, Vol. 128, *Mass Ejection from Active Galactic Nuclei*, ed. N. Arav, I. Shlosman, & R. J. Weymann, 13–+
- Bautista, M. A., Dunn, J. P., Arav, N., Korista, K. T., Moe, M., & Benn, C. 2010, *ApJ*, 713, 25
- Borguet, B. C. J., Arav, N., Edmonds, D., Chamberlain, C., & Benn, C. 2013, *ApJ*, 762, 49
- Borguet, B. C. J., Edmonds, D., Arav, N., Benn, C., & Chamberlain, C. 2012a, *ApJ*, 758, 69
- Borguet, B. C. J., Edmonds, D., Arav, N., Dunn, J., & Kriss, G. A. 2012b, *ApJ*, 751, 107
- Cattaneo, A., et al. 2009, *Nature*, 460, 213
- Churchill, C. W., Mellon, R. R., Charlton, J. C., Jannuzi, B. T., Kirhakos, S., Steidel, C. C., & Schneider, D. P. 1999, *ApJ*, 519, L43
- Ciotti, L., Ostriker, J. P., & Proga, D. 2009, *ApJ*, 699, 89
- . 2010, *ApJ*, 717, 708
- Costantini, E., et al. 2007, *A&A*, 461, 121
- Dai, X., Shankar, F., & Sivakoff, G. R. 2008, *ApJ*, 672, 108
- . 2012, *ApJ*, 757, 180
- Danforth, C. W., Keeney, B. A., Stocke, J. T., Shull, J. M., & Yao, Y. 2010, *ApJ*, 720, 976
- de Kool, M., Arav, N., Becker, R. H., Gregg, M. D., White, R. L., Laurent-Muehleisen, S. A., Price, T., & Korista, K. T. 2001, *ApJ*, 548, 609
- de Kool, M., Becker, R. H., Gregg, M. D., White, R. L., & Arav, N. 2002a, *ApJ*, 567, 58
- de Kool, M., & Begelman, M. C. 1995, *ApJ*, 455, 448

- de Kool, M., Korista, K. T., & Arav, N. 2002b, *ApJ*, 580, 54
- Di Matteo, T., Springel, V., & Hernquist, L. 2005, *Nature*, 433, 604
- Dixon, W. V., et al. 2007, *PASP*, 119, 527
- Dunn, J. P., Arav, N., Aoki, K., Wilkins, A., Laughlin, C., Edmonds, D., & Bautista, M. 2012, *ApJ*, 750, 143
- Dunn, J. P., Crenshaw, D. M., Kraemer, S. B., & Tripp, M. L. 2010a, *ApJ*, 713, 900
- Dunn, J. P., et al. 2010b, *ApJ*, 709, 611
- Edmonds, D., et al. 2011, *ApJ*, 739, 7
- Elvis, M. 2006, *Mem. Soc. Astron. Italiana*, 77, 573
- Faucher-Giguère, C.-A., Quataert, E., & Murray, N. 2012, *MNRAS*, 420, 1347
- Ferland, G. J., Korista, K. T., Verner, D. A., Ferguson, J. W., Kingdon, J. B., & Verner, E. M. 1998, *PASP*, 110, 761
- Gabel, J. R., Arav, N., & Kim, T. 2006, *ApJ*, 646, 742
- Gabel, J. R., et al. 2003, *ApJ*, 583, 178
- . 2005a, *ApJ*, 631, 741
- . 2005b, *ApJ*, 623, 85
- Ganguly, R., & Brotherton, M. S. 2008, *ApJ*, 672, 102
- Ganguly, R., Eracleous, M., Charlton, J. C., & Churchill, C. W. 1999, *AJ*, 117, 2594
- Ganguly, R., Sembach, K. R., Tripp, T. M., Savage, B. D., & Wakker, B. P. 2006, *ApJ*, 645, 868
- Germain, J., Barai, P., & Martel, H. 2009, *ApJ*, 704, 1002

- Hall, P. B., et al. 2002, *ApJS*, 141, 267
- Hamann, F., Barlow, T. A., Beaver, E. A., Burbidge, E. M., Cohen, R. D., Junkkarinen, V., & Lyons, R. 1995, *ApJ*, 443, 606
- Hamann, F., Barlow, T. A., Junkkarinen, V., & Burbidge, E. M. 1997, *ApJ*, 478, 80
- Hamann, F., & Ferland, G. 1993, *ApJ*, 418, 11
- Hamann, F. W., Barlow, T. A., Chaffee, F. C., Foltz, C. B., & Weymann, R. J. 2001, *ApJ*, 550, 142
- Hamann, F. W., Netzer, H., & Shields, J. C. 2000, *ApJ*, 536, 101
- Hewett, P. C., & Foltz, C. B. 2003, *AJ*, 125, 1784
- Holczer, T., Behar, E., & Kaspi, S. 2007, *ApJ*, 663, 799
- Hopkins, P. F., & Elvis, M. 2010, *MNRAS*, 401, 7
- Hopkins, P. F., Hernquist, L., Cox, T. J., Di Matteo, T., Robertson, B., & Springel, V. 2006, *ApJS*, 163, 1
- Hopkins, P. F., Murray, N., & Thompson, T. A. 2009, *MNRAS*, 398, 303
- Knigge, C., Scaringi, S., Goad, M. R., & Cottis, C. E. 2008, *MNRAS*, 386, 1426
- Korista, K. T., Bautista, M. A., Arav, N., Moe, M., Costantini, E., & Benn, C. 2008, *ApJ*, 688, 108
- Korista, K. T., et al. 1992, *ApJ*, 401, 529
- Levine, R., & Gnedin, N. Y. 2005, *ApJ*, 632, 727
- Maiolino, R., et al. 2012, *MNRAS*, 425, L66
- Mathews, W. G., & Ferland, G. J. 1987, *ApJ*, 323, 456

- Moe, M., Arav, N., Bautista, M. A., & Korista, K. T. 2009, *ApJ*, 706, 525
- Murray, N., Chiang, J., Grossman, S. A., & Voit, G. M. 1995, *ApJ*, 451, 498
- Muzahid, S., Srianand, R., Arav, N., Savage, B. D., & Narayanan, A. 2013, *MNRAS*, 431, 2885
- Muzahid, S., Srianand, R., Savage, B. D., Narayanan, A., Mohan, V., & Dewangan, G. C. 2012, *MNRAS*, 424, L59
- Netzer, H., et al. 2003, *ApJ*, 599, 933
- Osterman, S., et al. 2010, arXiv:1012.5827 [astro-ph.IM]
- Ostriker, J. P., Choi, E., Ciotti, L., Novak, G. S., & Proga, D. 2010, *ApJ*, 722, 642
- Petitjean, P., & Srianand, R. 1999, *A&A*, 345, 73
- Proga, D., Stone, J. M., & Kallman, T. R. 2000, *ApJ*, 543, 686
- Scannapieco, E., & Oh, S. P. 2004, *ApJ*, 608, 62
- Schlegel, D. J., Finkbeiner, D. P., & Davis, M. 1998, *ApJ*, 500, 525
- Scott, J. E., et al. 2004, *ApJS*, 152, 1
- Silk, J., & Rees, M. J. 1998, *A&A*, 331, L1
- Steenbrugge, K. C., et al. 2005, *A&A*, 434, 569
- Telfer, R. C., Kriss, G. A., Zheng, W., Davidsen, A. F., & Green, R. F. 1998, *ApJ*, 509, 132
- Telfer, R. C., Zheng, W., Kriss, G. A., & Davidsen, A. F. 2002, *ApJ*, 565, 773
- Wampler, E. J., Chugai, N. N., & Petitjean, P. 1995, *ApJ*, 443, 586